Dose-to-outcome modeling for lung robotic stereotactic body radiation therapy.

Veng Jean Heng

Medical Physics Unit
McGill University, Montreal

Montreal, Quebec

August 2019

A thesis submitted to McGill University in partial fulfillment of the requirements of the degree of Master of Science in Medical Radiation Physics

ACKNOWLEDGEMENTS

The work described in this thesis was only possible thanks to the help of several individuals. First and foremost, I would like to thank my supervisor Jan Seuntjens for the design of this project and for his valuable guidance and support throughout this year. I would also like to thank my fellow labmate André Diamant. This project would not have been conceptualized without his prior work on distant metastasis in conventional SBRT lung patients. The numerous discussions we've had during our collaboration have been extremely insightful. I would also like to thank him for providing the initial code for the dosimetric analysis in regions outside the PTV. Both his and Avishek Chatterjee's input have been of great help for my statistical analysis work. I would like to express my deepest gratitude to Marc-André Renaud for his instrumental support, without which this work would never have been possible. Being able to rely on his experience with the EGSnrc code and in beam modelling have made my introduction to the Monte Carlo world a painless one. Much of my work could only be done within this short year thanks to his design of the web-based TPS Radify and his PyRad code. I would also like to thank Houda Bahig for providing me with the patient data and François DeBlois for allowing me to retrieve patient plans for this study. I would like to further thank Karim Zerouali for his input on the CyberKnife beam model and Robert Doucet for our discussions on CyberKnife treatment planning. I would like to thank all the staff in the McGill Medical Physics Unit and in particular Piotr Pater and Russell Ruo for their help in obtaining beam commissioning measurements of the CyberKnife. A big thank you to Margery Knewstubb and Tatjana Nisic for taking care of all my administrative issues. Finally, I would also like to thank every student in the Medical Physics Unit for creating such a welcoming and friendly work environment. I would like to acknowledge funding by the CREATE Medical Physics Research Training Network [grant number 432290] and NSERC RGPIN-2014-06475. Finally, I am grateful for the monumental support of my parents and sister throughout all my studies.

ABSTRACT

The Ray-Tracing algorithm is a fast factor-based dose calculation method for the CyberKnife system. It however has been known to severely overestimate the dose to the target in lung plans. In this work, a cohort of 219 lung CyberKnife plans are recalculated with a completely independent Monte Carlo method. The beam model of the CyberKnife used in this work was built and tuned to match commissioning measurements. The original treatment planning dose, calculated with either Ray-Tracing or Monte Carlo, were compared to their recalculation. Target doses calculated with Ray-Tracing were found to significantly differ from their Monte Carlo recalculation. When correcting for tissue heterogeneities, Ray-Tracing was found to have a median overestimation of target doses by 29% (in EQD2). Without heterogeneity corrections, the discrepancy between Ray-Tracing and Monte Carlo doses were found to be highly variable, with target mean dose underestimated by up to 22% and overestimated by up to 72%. Over the entire cohort, this has caused a deterioration in target coverage, with only 27% of plans meeting their original prescription dose when re-assessed with their Monte Carlo recalculation. Differences in the dose to most organs-at-risk do not generally cause them to exceed their original dose limits. This only happens in at most 7% of plans (for the rib). The median difference between the dose-to-water and the dose-to-medium for various organs was found to be less or equal to 1%.

Despite the low compliance rate to the original prescription dose, this failure in target coverage was not found to be directly associated to lower loco-regional control rates. Target coverage by higher absolute doses were however correlated with superior loco-regional progression-free survival ($p = 0.027$) with a hazard ratio of 3.28 (95%CI:1.07-9.97). This result highlights the importance of delivering a sufficient dose to the target in order to achieve a better tumor control. Although a previous study had demonstrated a correlation between the dose outside the PTV and the incidence rate of distant metastasis in lung SBRT patients treated with conventional linacs, this correlation was not observed in the present CyberKnife

cohort. This is hypothesised to be due to the slower dose fall-off of CyberKnife doses when averaged isotropically outside the PTV.

ABRÉGÉ

L'algorithme Ray-Tracing du CyberKnife est une méthode de calcul de dose rapide en grande partie dû à sa simplicité. Cependant, plusieurs études ont démontré que cet algorithme surestime la dose au volume cible prévisionel (PTV) lorsqu'il est utilisé pour les plans de traitement du cancer du poumon. Dans le cadre de ce project, 219 plans de traitement CyberKnife du cancer du poumon ont été recalculé à l'aide d'un modèle Monte Carlo indépendant. Le modèle du faisceau du CyberKnife à été construit de manière à correpondre aux mesures d'étalonnage de la machine. La dose initiale calculée durant la planification de traitement, soit par méthode Ray-Tracing ou Monte Carlo, a été comparée à leur recalcul Monte Carlo. Nous constatons que la dose à la cible calculée par Ray-Tracing diffère significativement de la dose calculée par Monte Carlo. En effet, lorsque les corrections tenant compte de l'hétérogénéité de densité des tissus étaient utilisées, l'algorithme Ray-Tracing surestimait la dose à la cible par un facteur médian de 29%. Sans corrections d'hétérogénéité, nous constatons une plus grande variabilité dans cette différence entre Ray-Tracing et Monte Carlo. La dose à la cible calculée par Ray-Tracing pouvait être sous-estimée de 22% ainsi que surestimée de 72% dans les cas extrêmes. En analysant les doses recalculées, seulement 27% des plans de traitement étaient conformes aux doses originellement prescrites. Néanmoins, pour la plupart des organes à risque, la dose Monte Carlo n'excède pas leur limite respective. Le pire scénario est observé dans le cas des côtes où 7% des plans dépassent la dose limite associée. La différence médiane entre la dose absorbée à l'eau et la dose absorbée au milieu sont égales à 1% ou moins dans tous les organes étudiés.

Bien que le taux de conformité à la dose prescrite soit bas, la conformité en elle-même par la dose Monte Carlo n'a pas pu être associée à de meilleur taux de contrôle locorégional. Cependant le dosage absolu de la cible a été positivement corrélé avec le taux de contrôle locorégional ($p = 0.027$). Ce résultat souligne l'importance de délivrer une dose suffisante à la cible afin de maximiser le contrôle de la tumeur. Bien qu'une étude précédante ait demontré

une corrélation entre la dose en dehors du PTV and le taux d'apparition de métastases à distance pour des patients du cancer du poumon traités par radiothérapie stéréotaxique, cette corrélation n'a pas été observée dans la présente étude. L'absence de cette corrélation chez les patients du CyberKnife pourrait être en raison de la plus grande dose que celle-ci délivre en dehors du PTV.

TABLE OF CONTENTS

ACKNOWLEDGEMENTS ii

ABSTRACT iii

ABRÉGÉ v

LIST OF FIGURES ix

LIST OF TABLES xii

LIST OF ABBREVIATIONS xiii

CONTRIBUTION OF AUTHORS xv

1 Introduction 1

1.1 Cancer and Radiation Therapy 1
1.2 Thesis motivation and aims 3

2 Theory 9

2.1 Particle Interactions in Radiation Therapy 9
2.1.1 Electron Interactions 9
2.1.2 Photon Interactions 11
2.2 External Beam Radiation Therapy 14
2.2.1 Conventional Linear Accelerators 16
2.2.2 CyberKnife 19
2.3 Dosimetric Quantities 20
2.3.1 Depth doses 21
2.3.2 Off-center ratios 22
2.3.3 Output factors 22
2.3.4 Dose-volume histograms 22
2.4 Dose Calculation Methods 23
2.4.1 Ray-Tracing 24
2.4.2 Monte Carlo 26
2.5 Stereotactic Body Radiation Therapy 28

3 Large-scale dosimetric assessment of Monte Carlo recalculated doses for lung robotic stereotactic body radiation therapy 35

3.1 Abstract 35

3.2 Introduction . . . 36
3.3 Materials and Methods . . . 37
3.3.1 EGSnrc model . . . 37
3.3.2 Patient set . . . 39
3.3.3 Plan recalculation and analysis . . . 40
3.4 Results . . . 42
3.4.1 EGSnrc model validation . . . 42
3.4.2 Dosimetric characteristics . . . 44
3.4.3 Dose-to-medium . . . 46
3.5 Discussion . . . 48
3.6 Conclusions . . . 51
3.7 Acknowledgements . . . 52

4 Correlation between dose distal to the target and distant metastasis incidence rate for CyberKnife lung patients . . . 57

4.1 Preface . . . 57
4.2 Methods . . . 58
4.3 Results . . . 60
4.4 Discussion . . . 62

5 Conclusion . . . 66

LIST OF FIGURES

Figure page

1–1 Definitions of the different target volume delineations 3

2–1 Schematic diagram of Compton scattering. Taken from [1] 12

2–2 Dominance of the major photon interactions as a function of photon energy and medium atomic number. Bold curves represent the region where the two neighbouring dominant interactions have equal mass attenuation coefficient. Taken from [1] 14

2–3 Mass attenuation coefficient of each photon interaction in water. Coherent and incoherent scattering refer to Rayleigh and Compton scattering respectively. This graph was generated by the XCOM database [2]. 15

2–4 Schematic diagram of megavoltage linear accelerator. From [1] 17

2–5 Varian's Millenium 120 Multileaf collimator. From Varian Medical Systems . 18

2–6 CyberKnife M6 model at the McGill University Health Centre. 19

2–7 Diagram depicting distinction between a SSD vs. SAD setup. Taken from [3]. 21

2–8 Example of a cumulative DVH curve for a lung CyberKnife treatment plan. The curve was generated using Radify. Target structures ("PTV" and "IGTV") usually have 100% of their volume receiving high doses or more, whereas organs-at-risk are required to not receive more than a dose limit to more than a small fraction of their volume. 23

2–9 The Effective Path Length (EPL) converts the physical depth in patients into an equivalent depth in a homogeneous water phantom. EPL $= (1\text{ cm} \cdot 1) + (2\text{ cm} \cdot 0.5) = 2$ cm. 25

2–10 Idealistic relationship of TCP (A) and the probability of complications in normal tissue (B) with dose. The TCP curve is characterised by a large gradient region followed by a plateau. In the high dose plateau region, linear increase in dose have limited impact on tumour control. Figure taken from [1] 30

3–1 OCR for all 12 collimators (5, 7.5, 10, 12.5, 15, 20, 25, 30, 35, 40, 50 and 60 mm diameter). Although an offset is present in the shoulder of the largest collimator profile (60 mm), that collimator was not used in CyberKnife treatment plans. For clarity, the local residuals are only plotted for the 30 mm collimator (orange), which was the the most often used collimator in this study. 43

3–2 TMR for the 60 mm collimator up to 30 cm depth. Type A uncertainties of Monte Carlo doses are shown in the local residual plot. 44

3–3 Output factor for all collimator sizes. Agreement between MC calculation and measurement is observed within 1%. 44

3–4 Scatter plot of mean dose to the PTV as recalculated by EGSnrc against the TPS dose. Plans were separated according to the method with which the doses were calculated. Points close to the line of identity have similar TPS and EGSnrc recalculated mean PTV dose. 45

3–5 Scatter plot of the ratio of RAT-calculated to EGSnrc-calculated D_{mean} as a function of PTV volume. A Spearman correlation of -0.29 ($p < 10^{-4}$) suggests an inverse correlation between the RAT/EGSnrc PTV dose ratio and the PTV's size. 45

3–6 PTV coverage parameters for all 219 patient plans, based on MC-recalculated dose distributions. The target coverage goal of $D_{95\%} \geq$ Prescription Dose (PD) is only achieved in 27% of the plans when assessed on MC doses. . . 46

3–7 Loco-regional progression-free survival rate as a function of post-treatment days. Notches in the plot represent censoring due to lack of further of follow-ups. Shaded areas represent the 95% confidence band. The p-value of a log-rank test between the two curves is given. 47

3–8 Near-maximum $D_{2\%}$ doses delivered to OAR as recalculated by EGSnrc MC. For the lung, it is the fraction V_{20Gy} of lung volume receiving at least 20 Gy that is reported. Plans were separated according to their number of fractions to reflect the different dose limits of each fractionation scheme. Outliers are represented by crosses. The dose line corresponding to the normal tissue dose limits used for planning are drawn. Two patients had treatments delivered in 8 fractions and were not included in this plot. . . . 47

3–9 Ratios of dosimetric parameters as calculated using dose-to-medium to the same parameters using dose-to-water. Note that for the lung, it is a ratio of volumes and not doses that is shown. For OAR points, only plans where the OAR received $D_{2\%} \geq 4$ Gy, and therefore sufficiently small statistical uncertainty, were plotted. For similar reasons, if 2% of the OAR volume was smaller than 0.03 cm^3, the maximum dose deposited in at least 0.03 cm^3 was instead recorded. 49

4–1 Example of the generation of a $\mathrm{ROI}_{\mathrm{cont}}(x)$. The green region corresponds to voxels inside the PTV. Black lines refer to the convex hull grown isotropically about the PTV. The red region corresponds to the $\mathrm{ROI}_{\mathrm{cont}}(x)$: all voxels that are both inside the lung and between the PTV and the grown hull. 59

4–2 The mean dose to $\mathrm{ROI}_{\mathrm{cont}}(x)$ as a function of distance x beyond the PTV from 1 to 40 mm. The red points represent the mean dose averaged over patients who developed DM while blue points are averaged over patients who did not have DM. The error bars are calculated as the standard error on the subset-averaged mean with $k = 2$. Thus both curves overlap each other at the 95% confidence level. 60

4–3 The mean EQD2 to ROI as a function of distance x from the PTV. The dose to regions outside the PTV in CyberKnife plans (blue) is significantly larger than VMAT/CRT plans (red) for $x > 10$ mm, despite having similar dose in the PTV at the 95% confidence level. This figure is extracted from [2], where Gy_2 is a Gy in EQD2. 61

4–4 Histogram of the mean EQD2 to $\mathrm{ROI}_{\mathrm{cont}}(30)$ for CyberKnife (blue) and VMAT/CRT (red) plans. The threshold dose hypothesized in the previous study is represented by a black line. This figure is extracted from [2]. 62

4–5 Sagittal slice of the dose distribution in a typical CyberKnife (left) vs. a CRT plan (right). The red contour represents the PTV. The dose in the CRT plan is limited to slices near the PTV. This figure was produced by viewing the patients' dose distribution on Radify. 63

LIST OF TABLES

Table page

3–1 Patient set characteristics 39

LIST OF ABBREVIATIONS

CPE Charged-Particle Equilibrium.

CRT 3D Conformal Radiation Therapy.

CT Computed Tomography.

CTV Clinical Target Volume.

DM Distant Metastasis.

DVH Dose-Volume Histogram.

EBRT External Beam Radiation Therapy.

EPL Effective Path Length.

EQD2 Equivalent Dose in 2 Gy fractions.

GTV Gross Tumour Volume.

ICRU International Commission on Radiation Units and Measurements.

IMRT Intensity Modulate Radiation Therapy.

ITV Internal Target Volume.

linac Linear Accelerator.

MC Monte Carlo.

MLC Multileaf collimator.

MU Monitor Unit.

NSCLC Non-Small Cell Lung Cancer.

OAR Organs-At-Risk.

OCR Off-Center Ratio.

OF Output Factor.

PDD Percentage Depth Dose.

PTV Planning Target Volume.

RAT Ray-Tracing.

RED Relative Electron Density.

SAD Source-to-Axis Distance.

SBRT Stereotactic Body Radiation Therapy.

SSD Source-to-Surface Distance.

TCP Tumour Control Probability.

TMR Tissue-Maximum Ratio.

TPS Treatment Planning System.

VMAT Volumetric Arc Therapy.

CONTRIBUTION OF AUTHORS

This thesis contains one manuscript in preparation (Chapter 3): Veng Jean Heng, Marc-André Renaud, Robert Doucet, André Diamant, Houda Bahig, Jan Seuntjens, "*Large-scale dosimetric assessment of Monte Carlo recalculated doses for lung robotic stereotactic body radiation therapy*". I was responsible for all Monte Carlo simulation work, for all data analysis and for writing the manuscript. Marc-André Renaud provided assistance in setting up and post-processing Monte Carlo simulations, and reviewed the manuscript. Robert Doucet was responsible for the commissioning measurements of the CyberKnife and for the treatment planning of the cohort. André Diamant provided assistance for the statistical analysis and reviewed the manuscript. Houda Bahig, as the radiation oncologist responsible for the patient cohort, provided follow-up data. Jan Seuntjens was responsible for the design of this study and has reviewed the manuscript.

Part of the work described in Chapter 4 is also featured in a manuscript submitted for publication: André Diamant[1] , Veng Jean Heng[1] , Avishek Chatterjee, Sergio Faria, Houda Bahig, Edith Filion, Robert Doucet, Issam El Naqa, Jan Seuntjens, "*Does non-coplanar radiotherapy reduce distant recurrence in NSCLC patients compared to conventional SBRT?*" Manuscript submitted for publication (2019). Solely with respect to the content presented in this thesis, I was responsible for the analysis and generation of all CyberKnife-related data points. André Diamant was responsible for the analysis and generation of all VMAT/CRT data points and for the preparation of Fig.4–3 and 4–4. We jointly discussed our interpretation of the results. Avishek Chatterjee provided guidance for the statistical analysis. Houda Bahig and Sergio Faria provided patient follow-up data. André Diamant and Jan Seuntjens were both responsible for the design of this study.

[1] co-first author

CHAPTER 1
Introduction

1.1 Cancer and Radiation Therapy

In Canada, 30% of all deaths are due to cancer [1]. Lung cancer accounts for both the largest proportion of incidence rate (14%) and mortality (26%) among all cancer types. Four main cancer treatment modalities exist: surgery, chemotherapy, hormonal therapy and radiation therapy. Around half of all cancer patients typically have a treatment involving radiation therapy [2].

Cancer treatment by radiation therapy consists of depositing energy in the tumour through the use of ionizing radiation. A measure of the energy deposited in a given volume V is the absorbed dose D. It is defined as:

$$D = \frac{\mathrm{d}\bar{\epsilon}}{\mathrm{d}m}, \tag{1.1}$$

where $\bar{\epsilon}$ is the mean energy deposited by the ionizing radiation within the volume V of mass m. As such, it has units of joule per kilogram (J/kg), nominally defined to be the gray (Gy). The concept of the absorbed dose is central to radiation therapy. Delivering a larger dose to a cancer cell increases the probability of inducing DNA damage, thereby leading to cell death. However, healthy tissues are also susceptible to damage by ionizing radiation. The principal idea of radiation therapy thus consists of maximizing the dose to the targeted tumour while minimizing the dose to normal tissue. Through decades of treatments, different forms of radiation delivery have been devised to address this optimization problem. For superficial tumours, electron beams or low-energy orthovoltage X-rays are used to take advantage of their limited penetration depth. In brachytherapy, radioactive sources are placed inside the patient body in close proximity to the tumour. Today, the most widespread technique is External Beam Radiation Therapy (EBRT), where radiation beams are delivered from outside

the patient body.

The current workflow in a radiation oncology department can be described in 4 main steps. From a referral by a radiation oncologist, the treatment technique is chosen and the patient is prescribed a dose to their target tumour. A Computed Tomography (CT) scan of the patient must be taken in the same position as their desired treatment. A CT image consists of a 3D representation of the relative electron density map of the patient body, from which the tumour and other important organs can usually be distinguished. This step is called the CT simulation as the images are assumed to be representative of the patient at the time of their treatment. As such the imaging conditions are made to closely resemble the treatment conditions. Optical lasers and markers are used to ensure that the patient can be accurately re-positioned.

Contours of the target and Organs-At-Risk (OAR) are segmented on the CT images. They thus provide a binary information on the location of their respective structure within the images. There exist several delineations for the target shown in Fig.1–1. The Gross Tumour Volume (GTV) is limited to the grossly visible part of the tumour. The Clinical Target Volume (CTV) is an extension of the GTV such as to include the microscopic spread of the disease. The extent of the CTV depends on the clinical judgment of radiation oncologists as it is not simply discernible on the CT images. In other words, the CTV represents the region that must be treated by radiation. Beyond the CTV, an internal margin called the Internal Target Volume (ITV) is added to ensure that the CTV remains within the treated volume despite internal motion of the tumour due to physiological changes throughout the treatment course. An additional margin exists to take into account setup uncertainties when re-positioning the patient for treatment. This encompassing region consists of the Planning Target Volume (PTV), on which the prescribed dose is commonly optimized.

Using the contour information, the treatment beams are optimized on a patient-per-patient basis so as to take into account the patient anatomy featured in the CT images. During

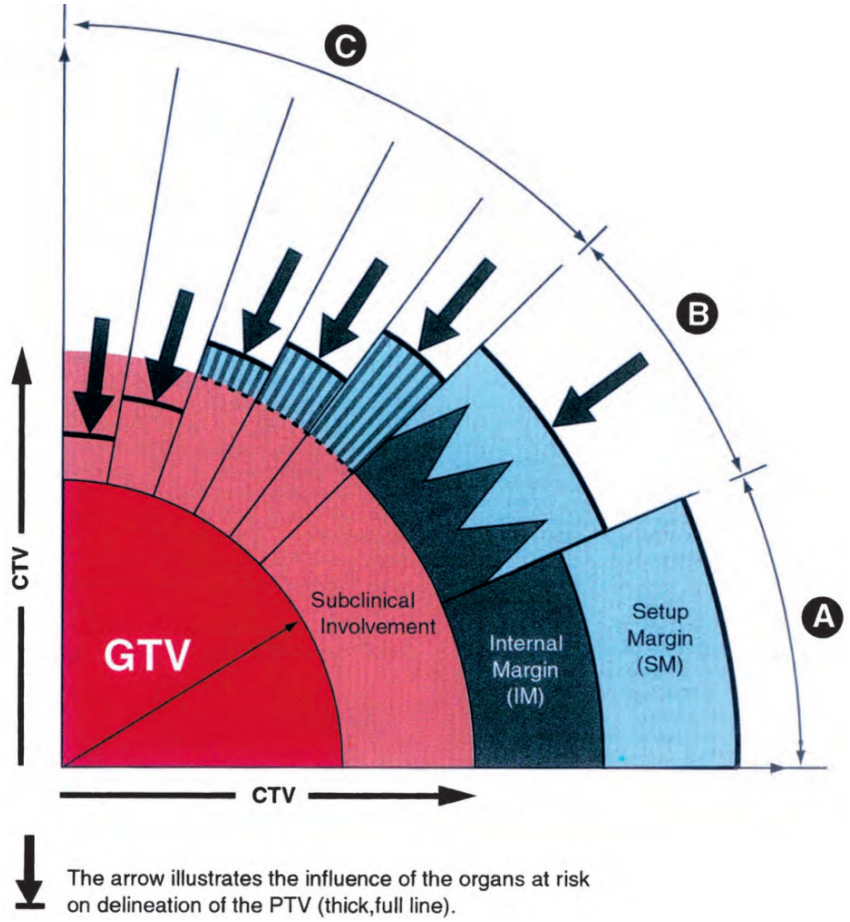

Figure 1–1: Definitions of the different target volume delineations. Taken from [3].

this step the important process of calculating the treatment planning dose is performed. Using its dose calculation algorithm, the Treatment Planning System (TPS) computes the necessary beam configuration and intensity to deliver the required prescription dose. The resulting dose distribution is a prediction of the dose to be delivered to the patient.

However, depending on the algorithm, this treatment planning dose may be more or less accurate. It also assumes that during the final step, which consists of the actual treatment delivery, the patient is static and positioned exactly as in the CT images over all treatment sessions.

1.2 Thesis motivation and aims

Today, Monte Carlo simulations provide the gold standard for accurate dose calculations. However, its computation time has historically been quoted to be prohibitive for regular use

within the clinical workflow [4]. As such, fast analytical techniques have been routinely used despite their inaccuracies in some scenarios. One such example is the Ray-Tracing (RAT) algorithm on the CyberKnife system (Accuray Inc., Sunnyvale, CA). Due to previous the lack of a more accurate dose calculation algorithm, RAT was initially used to calculate lung treatment plans. Numerous groups have investigated the accuracy of the RAT in heterogeneous sites like the lung and had found significant discrepancies from measurements. Wilcox et al. [5] performed film measurements of CyberKnife beams at depth in a heterogeneous slab phantom containing a lung-equivalent material. They found that RAT-predicted doses were consistently larger than their measured and Monte Carlo-calculated dose. In a follow-up study [6], they confirmed this overestimation to be also present in delivered patient plans. Similar results had been later observed by other groups [7]–[9]. Target coverage by the prescription dose was susceptible to significant deterioration if RAT plans are recalculated using Monte Carlo methods. Smaller size tumours were observed to be correlated with a larger discrepancy between RAT and Monte Carlo doses by van der Voort van Zyp et al. [10]. Historically, treatment plans were calculated without accounting for differences in density within the patient body. The patient is assumed to be a homogeneous phantom made out of water with unit density. Despite tissue heterogeneity correction methods being developed, the majority of the clinical experience at the time was based on prescription doses without heterogeneity corrections. Although the prescribed doses could differ significantly from the actually delivered dose [11], [12], they were resulting in satisfying patient outcomes for clinicians. As such, RTOG 0236 [13], one of the first lung Stereotactic Body Radiation Therapy (SBRT) clinical trials in North America, required lung patient plans to be calculated without heterogeneity corrections.

The purpose of this work was to assess accuracy of dose distributions calculated by the CyberKnife TPS. To do so, we compared the original dose distributions of CyberKnife plans to their recalculation using an independent Monte Carlo model. Although previous

studies have compared Ray-Tracing doses to the TPS Monte Carlo dose, they have only considered Ray-Tracing plans corrected for heterogeneity correction with the effective path length. In our work, both plans calculated with and without heterogeneity corrections were investigated. Plans originally calculated using the TPS Monte Carlo were also recalculated. With Monte Carlo being the dosimetric gold standard, the recalculated dose distribution is assumed to more closely reflect the actually delivered dose. Using a large set of 219 plans delivered on Non-Small Cell Lung Cancer (NSCLC) patients, we aimed to establish correlations between a patient's recalculated Monte Carlo dose and their loco-regional and distant outcome. This work can be split into three steps.

- A CyberKnife Monte Carlo beam model was built on EGSnrc[14] from scratch using technical drawings and geometrical measurements of the machine. The beam model is further tuned using commissioning measurements of the model that was used to treat patients in our cohort.
- Patient plans are extracted from the treatment planning archive system and replicated on EGSnrc for Monte Carlo recalculation. Relevant dosimetric parameters in the PTV and in organs-at-risk were calculated using both the original TPS dose and the recalculated dose.
- Parameters from the recalculated dose are used to investigate correlation with loco-regional control rates and incidence rates of distant metastasis.

REFERENCES

[1] Candian Cancer Statistics Advisory Committee. (2017). Canadian cancer statistics 2017, [Online]. Available: http://www.cancer.ca/~/media/cancer.ca/CW/cancer%20information/cancer%20101/Canadian%20cancer%20statistics/Canadian-Cancer-Statistics-2017-EN.pdf (visited on 07/02/2019).

[2] Canadian Partnership for Quality Radiotherapy. (2013). Patients and radiation treatment, [Online]. Available: http://www.cpqr.ca/for-patients/ (visited on 07/02/2019).

[3] T. Landberg, J. Chavaudra, J. Dobbs, *et al.*, "Report 62," *Journal of the International Commission on Radiation Units and Measurements*, vol. os32, no. 1, NP–NP, Apr. 2016, ISSN: 1473-6691. DOI: 10.1093/jicru/os32.1.Report62.

[4] K. Jabbari, "Review of fast monte carlo codes for dose calculation in radiation therapy treatment planning," *Journal of medical signals and sensors*, vol. 1, no. 1, pp. 73–86, 2011, ISSN: 2228-7477.

[5] E. E. Wilcox and G. M. Daskalov, "Accuracy of dose measurements and calculations within and beyond heterogeneous tissues for photon fields smaller than produced by cyberknife," *Medical Physics*, vol. 35, no. 6Part1, pp. 2259–2266, 2008. DOI: 10.1118/1.2912179.

[6] E. E. Wilcox, G. M. Daskalov, H. Lincoln, *et al.*, "Comparison of planned dose distributions calculated by monte carlo and ray-trace algorithms for the treatment of lung tumors with cyberknife: A preliminary study in 33 patients," *International Journal of Radiation Oncology*Biology*Physics*, vol. 77, no. 1, pp. 277–284, 2010, ISSN: 0360-3016. DOI: https://doi.org/10.1016/j.ijrobp.2009.08.001.

[7] M. B. Liu, N. C. Eclov, N. Trakul, *et al.*, "Clinical impact of dose overestimation by effective path length calculation in stereotactic ablative radiation therapy of lung

tumors," *Practical Radiation Oncology*, vol. 3, no. 4, pp. 294–300, 2013, ISSN: 1879-8500. DOI: https://doi.org/10.1016/j.prro.2012.09.003.

[8] V. W. Wu, K.-w. Tam, and S.-m. Tong, "Evaluation of the influence of tumor location and size on the difference of dose calculation between ray tracing algorithm and fast monte carlo algorithm in stereotactic body radiotherapy of non-small cell lung cancer using cyberknife," *Journal of Applied Clinical Medical Physics*, vol. 14, no. 5, pp. 68–78, 2013. DOI: 10.1120/jacmp.v14i5.4280.

[9] S. E. Braunstein, S. A. Dionisio, M. W. Lometti, *et al.*, "Evaluation of ray tracing and monte carlo algorithms in dose calculation and clinical outcomes for robotic stereotactic body radiotherapy of lung cancers," *J Radiosurg SBRT*, vol. 3, no. 1, pp. 67–79, 2014, ISSN: 2156-4639.

[10] N. C. van der Voort van Zyp, M. S. Hoogeman, S. van de Water, *et al.*, "Clinical introduction of monte carlo treatment planning: A different prescription dose for non-small cell lung cancer according to tumor location and size," *Radiotherapy and Oncology*, vol. 96, no. 1, pp. 55–60, 2010, ISSN: 0167-8140. DOI: https://doi.org/10.1016/j.radonc.2010.04.009.

[11] Y. Xiao, L. Papiez, R. Paulus, *et al.*, "Dosimetric evaluation of heterogeneity corrections for rtog 0236: Stereotactic body radiotherapy of inoperable stage i-ii non-small-cell lung cancer," *Int J Radiat Oncol Biol Phys*, vol. 73, no. 4, pp. 1235–1242, Mar. 2009, S0360-3016(08)03800-5[PII], ISSN: 1879-355X. DOI: 10.1016/j.ijrobp.2008.11.019.

[12] S. Ahmad, T. D. F. Herman, H. Gabrish, T. Herman, and M. Vlachaki, "Impact of tissue heterogeneity corrections in stereotactic body radiation therapy treatment plans for lung cancer," *Journal of Medical Physics*, vol. 35, no. 3, p. 170, 2010. DOI: 10.4103/0971-6203.62133.

[13] R. Timmerman, R. Paulus, J. Galvin, *et al.*, "Stereotactic Body Radiation Therapy for Inoperable Early Stage Lung Cancer," *JAMA*, vol. 303, no. 11, pp. 1070–1076, Mar. 2010, ISSN: 0098-7484. DOI: 10.1001/jama.2010.261.

[14] I. Kawrakow and D. W.O. Rogers, "The egsnrc code system: Monte carlo simulation of electron and photon transport," Jan. 2000.

CHAPTER 2
Theory

In this chapter, an overview will be given on the fundamental theory behind the particle interactions that lead to the deposition of dose by ionizing radiation. The generation of these radiation in external beam radiation therapy will be explained by examining the relevant components of a medical linear accelerator. A few methods employed to calculate the dose delivered by these accelerators will be considered. Finally the basic radiobiology surrounding Stereotactic Body Radiation Therapy (SBRT) will be discussed.

2.1 Particle Interactions in Radiation Therapy

A radiation is said to be ionizing if it has the ability of causing the loss of an electron in an atom. Multiple processes can cause ionization but they ultimately result in a transfer of energy to a bound electron that is larger or equal to its binding energy. The minimum energy required to ionize an atom, i.e. the binding energy of its mostly loosely bound electron, is defined to be its ionization potential. Ionizing radiation can then be further divided in two categories: directly and indirectly ionizing radiation. As its name suggests, directly ionizing radiation are charged particles capable of depositing energy directly through Coulomb interaction with atomic electrons. In contrast, indirectly ionizing radiation, which are neutral particles such as photons and neutrons, must first release a charged particle through interactions with either orbital electrons or the nucleus of an atom. The released charged particles are the ones responsible for most of the energy deposition.

2.1.1 Electron Interactions

Electrons, like other light charged particles, interact with matter through the Coulomb force. The interaction can either occur with the orbital electrons or the nucleus of an atom depending on the impact parameter of the incident electron. For impact parameters that are on the order of the radius of the atom, the incident electron can be classically understood

to collide with an orbital electron, thus transferring a fraction of its energy. Depending on the magnitude of the energy transferred, the orbital electron can be either excited to a higher orbital state, or ejected out of the atom thus leading to ionization. If the impact parameter is much smaller than the radius of the atom, the incident electron is subjected to the electric field of the much heavier nucleus. As its trajectory gets deflected through Coulomb interactions, the electron suffers an acceleration and therefore loses energy through radiative emission of bremsstrahlung photons. The production of bremsstrahlung photons is governed by the Larmor relationship such that the power of emitted photons is proportional to the square of the acceleration of a charged particle. The energy of the emitted photons, defined to be X-rays, follows a continuous distribution with a maximum energy equal to the kinetic energy of the incident electron. Bremsstrahlung production is particularly important for the generation of X-rays in modern linear accelerators (see Section 2.2.1). The energy lost by charged particles traveling in matter can be quantified by the stopping power S:

$$S = -\frac{\mathrm{d}E_k}{\mathrm{d}x}, \tag{2.1}$$

defined to be the rate of kinetic energy E_k lost by the particle as a function of distance x. It follows that the mean path length travelled by the charged particle, defined to be the range R, can be approximated as the integral of the inverse of the stopping power over energy, representing a continuous slowing down from an initial energy E_{k_o} to 0:

$$R = -\int_{E_{k_o}}^{0} 1/S(E)\,\mathrm{d}E \tag{2.2}$$

The stopping power can be split as the sum of a collisional component S_{col} and a radiative component S_{rad} accounting for the contributions from the two different interactions. As only collisional interactions deposits energy to the medium near the point of interaction, the collisional stopping power S_{col} is related to dose as:

$$D = \phi S_{\mathrm{col}}/\rho, \tag{2.3}$$

where ϕ is the electron fluence and ρ is the mass density of the medium.

2.1.2 Photon Interactions

As opposed to charged particle interactions, there are many more ways for photons to interact with matter. Some of them result in the release of charged particles which in turn can deposit dose, while others only result in scattering of the photon. However, they all ultimately lead to an attenuation of the photon beam, dictated by the linear attenuation coefficient μ. Given a monoenergetic photon pencil beam of intensity I_o, its attenuation as it travels a distance x through a medium with linear attenuation coefficient μ is described by an exponential decay:

$$I(x) = I_o\, e^{-\mu x}. \tag{2.4}$$

The linear attenuation coefficient is related to the total photon cross-section in matter through the mass attenuation coefficient μ/ρ:

$$\frac{\mu}{\rho} = \sigma_{\text{tot}} \frac{N_A}{A}, \tag{2.5}$$

where N_A is the Avogadro constant and A is the atomic mass number. Therefore the linear attenuation coefficient represents the probability for a photon interaction to occur when travelling a unit distance x in matter. As the total photon cross-section is the sum of all the individual cross-sections for each possible interaction, it follows that the total mass attenuation coefficient is also the sum of the individual mass attenuation coefficient for each interaction type.

For a photon interacting with orbital electrons, where the photon energy $h\nu$ is larger or equal to the electron binding energy E_{B}, the photon can be absorbed by the electron through the photoelectric effect. The electron is then ejected out of the atom with a kinetic energy equal to: $E_k = h\nu - E_{\text{B}}$. The mass attenuation coefficient τ/ρ for this interaction to occur in a medium of atomic number Z is proportional to $(Z/h\nu)^3$.

As photons can also be viewed as electromagnetic waves, their interaction with tightly bound orbital electrons can cause them to oscillate such that the atom forms an oscillating dipole. The latter in turn re-emits photons at the same frequency as the incoming wave. This interaction, called Rayleigh scattering, can therefore be understood as an elastic scattering of the initial photon with the atom. Almost no energy is transferred and the orbital electrons return to their original state. As no charged particles are released, Rayleigh scattering is not responsible for any dose deposition. Its mass attenuation coefficient σ_R/ρ is proportional to $Z/(h\nu)^2$.

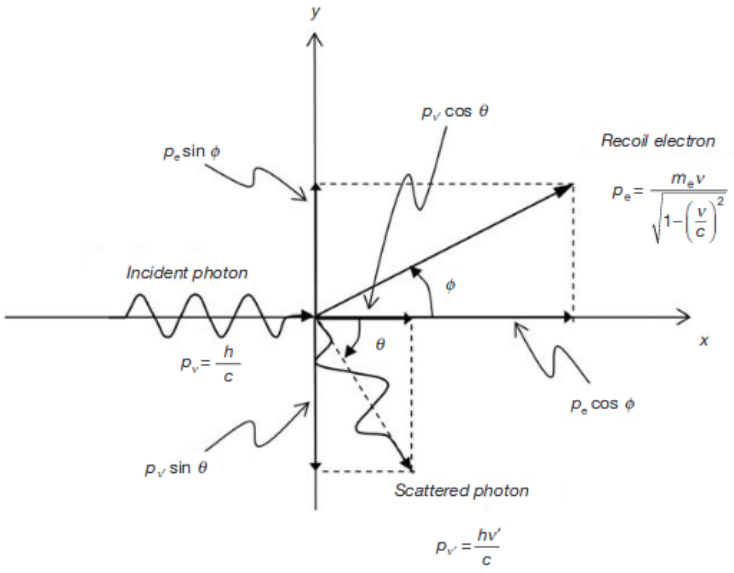

Figure 2–1: Schematic diagram of Compton scattering. Taken from [1]

If the energy of the incident photon $h\nu$ is much larger than the binding energy, its collision with an electron can cause it to be ejected out of the atom through Compton scattering, see Fig.2–1. Kinematics dictate that if the scattered photon has an energy $h\nu'$ the recoil electron must have an energy $E_k = h\nu - h\nu'$. Enforcing momentum and energy conservation laws lead us to a relationship between the scattering angles and the outgoing

energies:

$$h\nu' = h\nu \frac{1}{1 + \frac{h\nu}{m_e c^2}(1 - \cos\theta)} \tag{2.6}$$

$$E_k = h\nu \frac{\frac{h\nu}{m_e c^2}(1 - \cos\theta)}{1 + \frac{h\nu}{m_e c^2}(1 - \cos\theta)}, \tag{2.7}$$

where $m_e c^2$ is the electron rest mass energy, and θ is the photon scattering angle as shown in Fig.2–1. The mass attenuation coefficient σ_C/ρ for Compton scattering is independent of Z.

In the presence of a Coulomb field such as the one of a nucleus, a photon has a finite probability to transform into an electron-position pair through pair production. As mass is created in this interaction, the photon must have a minimum energy of $h\nu > 2m_e c^2 = 1.022$ MeV for it to occur. Kinematic laws require the presence of a third recoiling particle (the nucleus) for this pair production to be possible. This interaction can also occur near the field of an orbital electron, in which case it is called a triplet production: the orbital electron is also ejected with the recoil energy. The threshold photon energy for triplet production is however higher: $h\nu \geq 4m_e c^2$. The mass attenuation coefficient κ/ρ for pair production is approximately proportional to Z and is null for energies lower than the threshold.

The total mass attenuation coefficient is thus equal to:

$$\frac{\mu}{\rho} = \frac{\tau}{\rho} + \frac{\sigma_R}{\rho} + \frac{\sigma_C}{\rho} + \frac{\kappa}{\rho}. \tag{2.8}$$

The contribution from each interaction varies differently with photon energy and Z. The regions where each interaction dominates is given in Fig.2–2. For low atomic number, characteristic of the human body, and for energies used in radiation therapy (on the order of 1∼10 MeV), the Compton effect dominates photon interactions. As shown in the plot of mass attenuation coefficients in water (Fig.2–3), the contribution from Compton scattering represents the almost entirety of the total mass attenuation coefficient in that energy range.

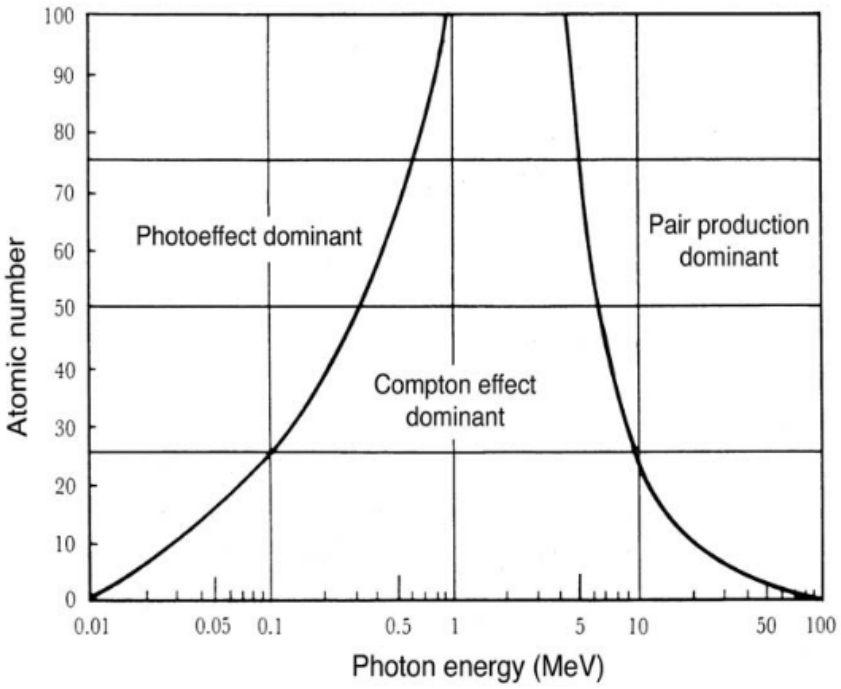

Figure 2–2: Dominance of the major photon interactions as a function of photon energy and medium atomic number. Bold curves represent the region where the two neighbouring dominant interactions have equal mass attenuation coefficient. Taken from [1]

.

As such, the mass attenuation coefficient in photon beam therapy is often treated to be independent of the atomic number Z.

2.2 External Beam Radiation Therapy

As discussed in the previous section, ionizing radiation can be used to deposit dose in patients through its different interactions. If one can accurately deliver the radiation to a tumour, local tumour control can be achieved. In External Beam Radiation Therapy (EBRT), the radiation is delivered from outside the patient body and, except for superficial tumours, travels through centimeters of healthy tissue before reaching the target. Electrons lose energy as they travel through more matter as expressed through the stopping power of the medium and photons are attenuated exponentially as described by the linear attenuation coefficient of the medium. As such for a single electron or photon beam, the dose deposited to a deep-seated tumour would be significantly less than the dose deposited to the tissue above it. However, if multiple beams are used from different angles such that they intersect

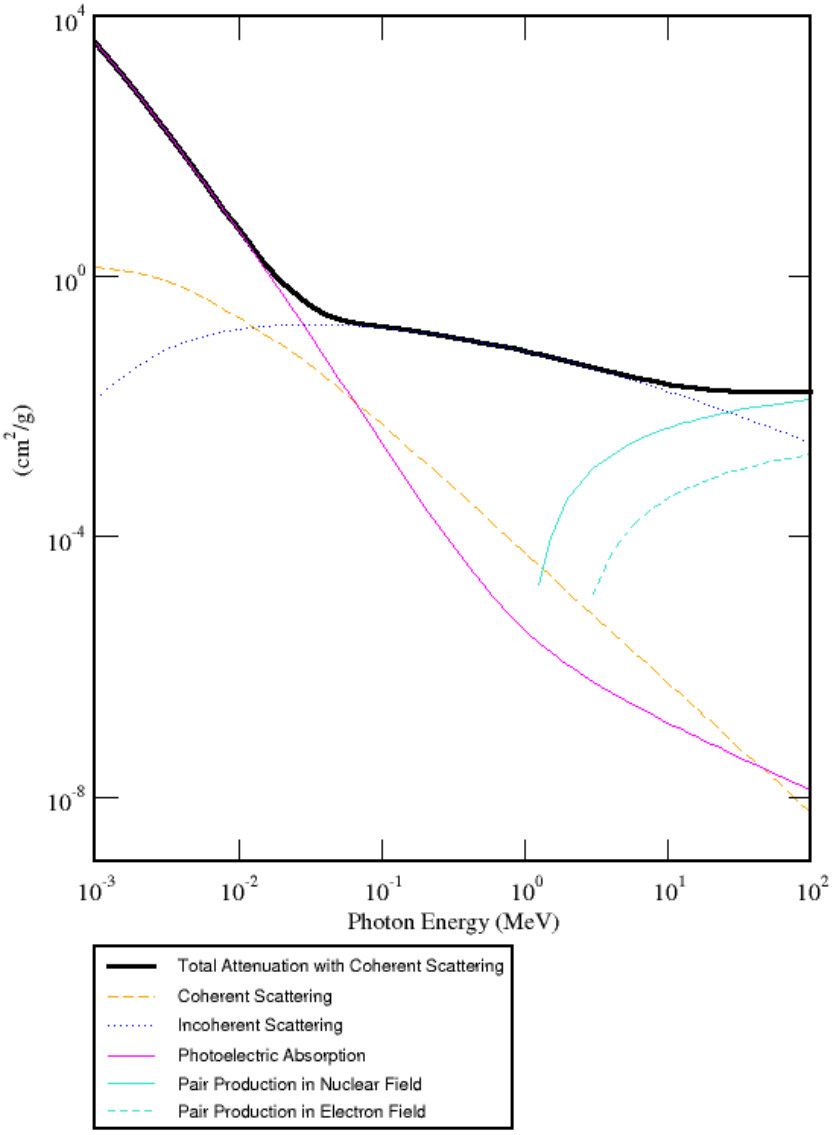

Figure 2–3: Mass attenuation coefficient of each photon interaction in water. Coherent and incoherent scattering refer to Rayleigh and Compton scattering respectively. This graph was generated by the XCOM database [2].

at the tumour location, the relative dose to the surrounding tissue can be made substantially lower.

2.2.1 Conventional Linear Accelerators

Delivery methods for EBRT have undergone numerous iterations, ranging from kilovoltage energy orthovoltage x-ray tubes during the early days of radiotherapy to current megavoltage accelerators. Conventional state-of-the-art medical Linear Accelerator (linac) all rely on the same principle to generate high energy particles: the acceleration of electrons through a waveguide. This fundamental design which started seeing broader clinical usage in the 1970's remains to this day the cornerstone of EBRT.

A schematic diagram of a megavoltage linac is shown in Fig.2–4. Electrons are initially generated in the electron gun by heating a filament cathode. As they are freed from the cathode by thermionic emission, they then drift towards the anode positioned at the entrance of the accelerating waveguide. True to its name, the accelerating waveguide is the principal component of the linac responsible for ramping up the electron kinetic energies from the keV range to MeVs. The waveguide itself is made out of cylindrical cavities equally spaced along its length. A microwave produced by a radiofrequency power generator is injected into the cavities so as to setup an electric field capable of accelerating electrons.

Upon reaching the end of the waveguide, now-MeV electrons are deflected towards a thick metallic slab using bending magnets. This slab is the target, which has the purpose of generating X-ray photons through bremsstrahlung. As the incident electrons pass through the target, they are subjected to the electromagnetic field of atomic nucleii within the latter. When decelerated, electrons emit a photon of energy equal to its lost kinetic energy. Although the incident electrons have mostly mono-energetic kinetic energies, bremsstrahlung photons are generated with a continuous spectrum of energy. Thus, a 6 MV linac will accelerate electrons to around 6 MeV and generate X-rays with energies between 0 and 6 MeV. The mean X-ray energy is around a third of the electron energy (e.g., 2 MeV for a 6 MV linac).

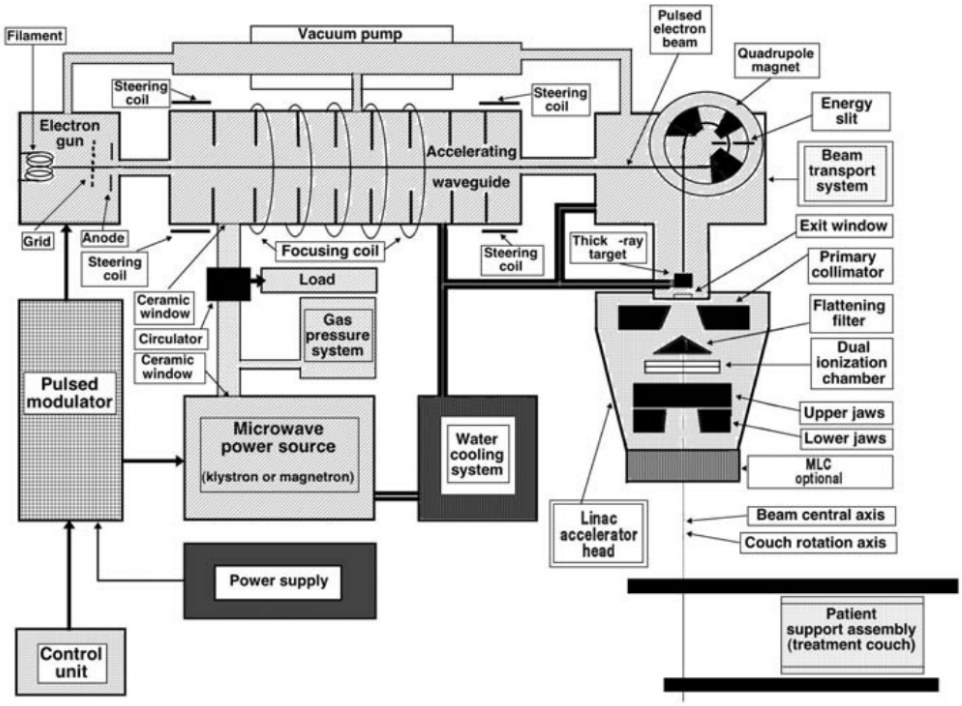

Figure 2–4: Schematic diagram of megavoltage linear accelerator. From [1]

The X-ray target and the following components constitute the linac treatment head. Primary collimators, usually made out of tungsten, initially shape the outgoing photon beam. These collimators are fixed and are therefore shaped to generate a beam broader than the maximum desired field size. A flattening filter is placed in the way of the beam and serves a dual purpose. Indeed, right before hitting the target, the initial electrons form a pencil beam. As they get scattered through the target, bremsstrahlung photons are preferentially generated towards the center of the field. This has the effect of creating an unbalanced field with a sharper intensity at the center. Shaped like a cone, the flattening filter resolves this issue by preferentially attenuating photons on paths near the center. Its second purpose is the origin of the second part of its name: further filtering electrons that have not been fully stopped by the target. For the purpose of generating electron beams, the target is removed and a thin scattering foil replaces the flattening filter. The foil scatters the incident electron pencil beam into a wider clinical beam. An ionization chamber allows the linac system to monitor the delivered dose. The response of the chamber is measured in monitor

units. At most institutions, it is regularly cross-calibrated with an external ionization chamber such that 1 Monitor Unit (MU) corresponds to 1 cGy in well-defined reference conditions.

The jaws or secondary collimators constitute the second component of the beam collimation system. Made out of similar material as the preceding collimators, the jaws can, however, be moved to specific locations during treatments to provide the desired beam field size. In most conventional linacs, there are two set of jaws: one for each axis of the field, thereby creating rectangular fields. For further collimation in custom field shapes, the usage of Multileaf collimator (MLC) is needed. Made out of retractable high Z thin leaves, the MLC allows the linac to shape its beam with higher resolution. The field can thus be made to fit the shape of the target tumour (see Fig.2–5).

In most modern linacs, the linac treatment head is attached to a gantry that is capable of

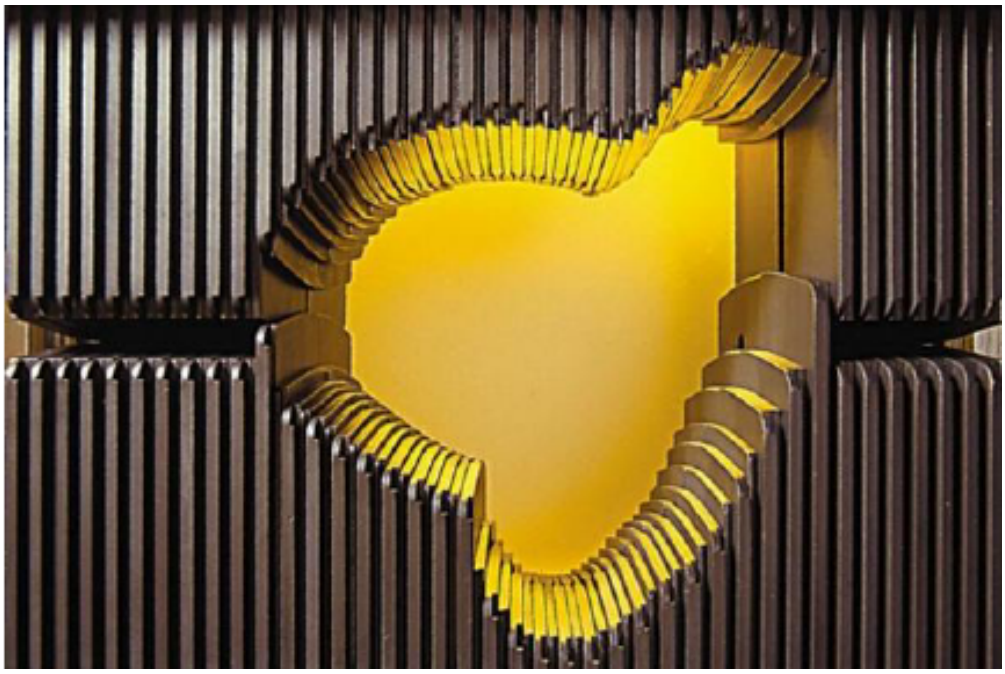

Figure 2–5: Varian's Millenium 120 Multileaf collimator. From Varian Medical Systems

360° rotation. As a result, in EBRT treatments, photon beams are commonly delivered at discrete angles of an arc or continuously over the latter.

2.2.2 CyberKnife

The CyberKnife (Accuray Inc., Sunnyvale, CA) is one such linac with a few unique characteristics. In essence, it is a 6 MV X-band linac which allows it to have a more compact form factor as shown in Fig.2–6. The electron gun, accelerating waveguide, target and beam collimation system are all setup linearly and the relatively low energy and higher RF frequency means that the waveguide can be made shorter than in conventional linacs. The CyberKnife also does not use a flattening filter, allowing for higher dose rate delivery. The distinctive feature of the CyberKnife is, however, in the stand of the linac: an industrial robotic arm. With 6 axes of rotation, the arm enables CyberKnife treatments to deliver photon beams from theoretically any angle. As opposed to conventional EBRT, CyberKnife treatment plans are therefore non-coplanar. Mathematically, this means that CyberKnife dose distributions can be made more conformal to the target at the expense of larger volumes of tissue exposed to low dose baths.

Figure 2–6: CyberKnife M6 model at the McGill University Health Centre.

Although a conformal dose distribution goes hand-in-hand with the radiation therapy philosophy of maximizing dose to targets while minimizing dose to healthy tissue, its sharp dose gradients, however, demand a stricter positional accuracy. Therein lies the second asset of the CyberKnife: its on-board kV imaging system. Two X-ray sources mounted on the ceiling (see Fig.2–6) are used before and during treatments to track target motion and automatically adjust treatment beam positions accordingly. Multiple tracking methods have been developed by Accuray. They either make use of existing anatomical contrasts such as between bone and soft-tissue by tracking the spine or the skull, or between lung tumours and lung tissue by tracking the tumour itself. If neither of these are reliable for the patient, fiducials can also be implanted. The optimal corrected treatment beam positions are then obtained by correlating target motion to the breathing pattern of the patient in real-time.

In the early models of the CyberKnife, the only beam collimation system available consisted of fixed conic collimators. They are a set of 12 tungsten cones which determine the field of the beam, ranging from 5 to 60 mm in diameter as projected to a Source-to-Axis Distance (SAD) of 80 cm. The CyberKnife system is programmed to autonomously switch between collimators by detaching and attaching them at the end of the linac head. Recent models have incorporated the Iris™ collimator which replicates the field created by the previous cones but using variable tungsten segments. Treatment time is thus saved as the collimators don't have to be physically reattached when changing field sizes. The M6 model of the CyberKnife has further introduced the InCise™ MLC, allowing for variable field shapes.

2.3 Dosimetric Quantities

To mathematically quantify the dose delivered to the patient, several quantities have been defined to characterise the dose deposition of a beam. A distinction must however be made between quantities defined in a constant Source-to-Surface Distance (SSD) setup and an isocentric (constant SAD) setup, see Fig.2–7. In an SSD setup the distance between the

source and the surface of the patient is always kept constant. The distance from the source to the point of interest varies with its depth. In an SAD setup, the point of interest is kept at the isocenter and constantly at the same distance from the source.

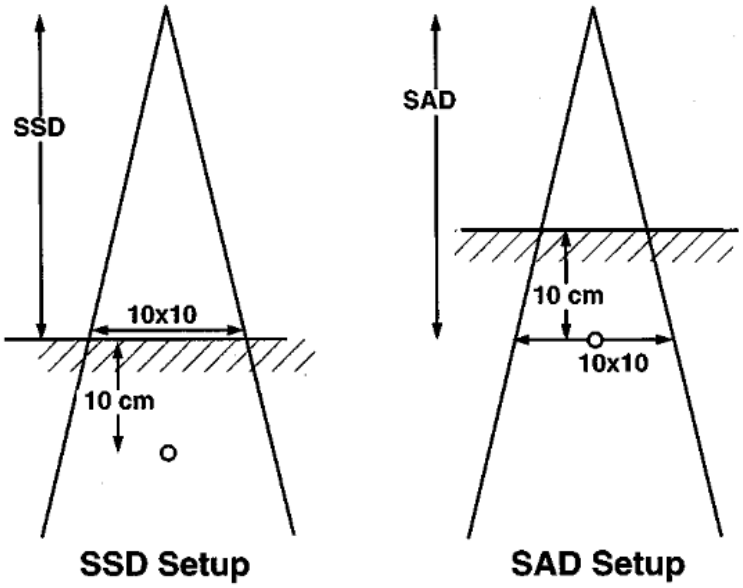

Figure 2–7: Diagram depicting distinction between a SSD vs. SAD setup. Taken from [3].

2.3.1 Depth doses

The variation of the dose deposition as a function of depth in a medium is quantified by the Percentage Depth Dose (PDD) and the Tissue-Maximum Ratio (TMR). They are both defined to be the ratio of the dose deposited on the central axis at a given depth d relative to the maximum dose (usually quoted in percent):

$$\mathrm{TMR}(d) = \frac{\mathrm{Dose}(d)}{\mathrm{Dose}(d_{max})}, \tag{2.9}$$

where d_{max}, is the depth of maximum dose. The PDD however assumes a constant SSD, such that the surface of the phantom is always at the same distance from the source for all dose points. The distance between the dose point and the source increases linearly with depth. In contrast, for the TMR, all dose points are at the same distance from the source. Thus, for a TMR measurement, the phantom is shifted at every measurement depth.

2.3.2 Off-center ratios

The dose off-axis is described by the Off-Center Ratio (OCR). It is defined, at a given depth d, as the ratio of the dose for a point at a distance r to the dose on the central axis:

$$\mathrm{OCR}(r, d) = \frac{\mathrm{Dose}(r, d)}{\mathrm{Dose}(0, d)} \tag{2.10}$$

2.3.3 Output factors

The Output Factor (OF) describes the variation in dose for differing field sizes. It is defined as the ratio of the dose on the central axis at the depth of maximum dose d_{max} for a given field size A to the dose at the same point for a reference field size A_{ref}:

$$\mathrm{OF}(A) = \frac{\mathrm{Dose}(A, r = 0, d = d_{max})}{\mathrm{Dose}(A_{ref}, r = 0, d = d_{max})}. \tag{2.11}$$

The reference field size is commonly taken to be 10×10 cm^2 for conventional linacs.

2.3.4 Dose-volume histograms

In radiation therapy, the primary concern is knowing the dose delivered to the target and each organ. However, these structures are not point-like but rather volumes, there is therefore a distribution of the dose within each structure. Thus, to characterize this dose distribution, the differential Dose-Volume Histogram (DVH) is a histogram of the dose, where frequency is normalized to the volume of the structure. A point on a differential DVH graph therefore represents the percentage of voxels (y-axis) within the structure that receives a given dose (x-axis). However, we are often more interested in knowing the fraction of the volume receiving a given dose *or more*. This tells us, for example, whether or not the target is being sufficiently covered, or whether a too large fraction of the lung is receiving a too high dose. As such, the cumulative DVH is more commonly used: it is defined as the reverse cumulative histogram of the dose in a structure. For a dose of interest (x-axis), the corresponding point on a cumulative DVH curve is the integral (y-axis) of the differential DVH curve from the maximum dose to the dose of interest. The cumulative DVH curve therefore represents the percentage of volume receiving *at least* a given dose as a function of dose. An

example of such curve can be found in Fig.2–8.

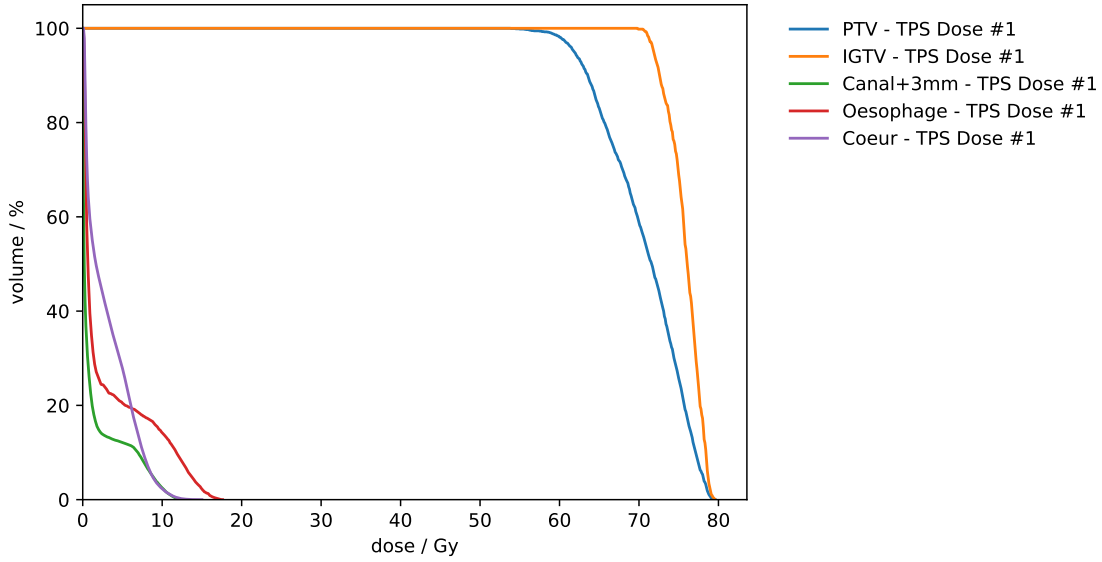

Figure 2–8: Example of a cumulative DVH curve for a lung CyberKnife treatment plan. The curve was generated using Radify. Target structures ("PTV" and "IGTV") usually have 100% of their volume receiving high doses or more, whereas organs-at-risk are required to not receive more than a dose limit to more than a small fraction of their volume.

The DVH curve gives rise to two important quantities which are the dose $D_{v\%}$ delivered to at least $v\%$ of a structure's volume and the percentage $V_{D\text{Gy}}$ of a structure's volume receiving at least D Gy. [1]

2.4 Dose Calculation Methods

In order to create a treatment plan, the TPS must be able to predict the dose distribution in a patient for a given linac configuration. Starting out as hand calculations, dose calculation methods have improved significantly over the years, in large part thanks to advancements in computational power. Different types of calculation methods exist, ranging from simple table lookups of in-water measurements to full stochastic simulations of particle transports and

[1] Note that these concepts are also defined for absolute volumes (e.g., D_{vcm^3}) or relative dose, e.g., $V_{D\%}$

interactions. Superior accuracy in the dose model often implies more computational time. According to the International Commission on Radiation Units and Measurements (ICRU), dose calculation methods can be separated into two large categories: factor-based methods and model-based methods [4]. In this section, an overview of the two dose calculation methods available on the CyberKnife system will be given.

2.4.1 Ray-Tracing

The RAT algorithm is the first dose calculation method made available on the CyberKnife's treatment planning system. The way RAT calculates doses in patients is very similar to hand calculations. To do so, it requires 4 input parameters: the collimator size A_{col}, the shortest distance to the central axis R_{SAD}, SAD and the water-equivalent depth d_{eff} of the point of interest. The collimator size (5 to 60 mm) is defined as the nominal diameter of the field projected at a SAD of 80 cm. The water-equivalent depth of a point is its physical depth scaled by Relative Electron Density (RED) to water averaged over all voxels that lie on the line joining the dose point and the beam source. It is thus the "Effective Path Length (EPL)" in water through which travels the beam. The calculation of the EPL is demonstrated in Fig.2–9. The dose D at a point is then calculated by RAT using the following equation:

$$D = MU \cdot \text{OCR}(A_{\text{col}}, R_{80}, d_{\text{eff}}) \cdot \text{TMR}(A_{\text{SAD}}, d_{\text{eff}}) \cdot \text{OF}(A_{\text{col}}, \text{SAD}) \cdot (80/\text{SAD})^2, \qquad (2.12)$$

where $R_{80} = R_{\text{SAD}}(80/\text{SAD})$ and A_{SAD} is the field size at the dose calulation point. The OCR at a given depth and for a given collimator is the ratio of the dose at a given off-axis radius R_{80} to the dose on the central axis, both assumed to be at SAD = 80 cm. The TMR is the ratio of the dose at a given depth d_{eff} to the maximum dose on the central axis and at equal SAD = 80 cm. For the CyberKnife, the maximum dose is measured to be at $d_{\text{max}} = 1.5$ cm in water. The OF is defined to be the ratio of the maximum dose measured at d_{max} for a given collimator A_{col} to the maximum dose of the $A_{\text{col}} = 60$ mm collimator. The OCR, TMR and OF are measured in water at the commissioning of a CyberKnife machine and are

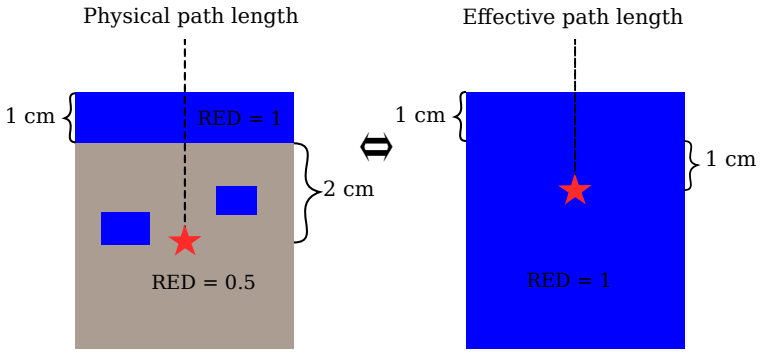

Figure 2–9: The EPL converts the physical depth in patients into an equivalent depth in a homogeneous water phantom. EPL $= (1\text{ cm} \cdot 1) + (2\text{ cm} \cdot 0.5) = 2$ cm.

then input into the TPS as tables. The RAT algorithm will then interpolate or extrapolate from these measurements to compute equation 2.12. All the previously mentioned quantities serve to convert the dose in reference conditions (80 cm SAD, $d_{\text{eff}} = 1.5$ cm, $A_{\text{col}} = 60$ mm) to the dose at the calculation point. The monitor unit (MU) can be understood as a scaling factor: 1 MU is calibrated for the CyberKnife to deliver 1 cGy in reference conditions.

The parameters that affect a dose calculation in RAT therefore only specify the geometric position of the point of interest along a ray line from the source. No information about the tissue surrounding the calculation point is considered if they do not intersect the ray line. After calculating d_{eff}, the problem is treated as if it is in a homogeneous water phantom. This method is a good approximation of the attenuation of the primary beam, and is very fast to calculate. In homogeneous regions like the brain, doses calculated by RAT are fairly accurate. However, if heterogeneities are present, such as in Fig.2–9, the different scatter contribution due to the heterogenity is completely ignored in the RAT calculation. Furthermore, a lower tissue density with respect to water will have a longer range of secondary electrons. As the field size is finite, this difference in electron range R can induce a loss in Charged-Particle Equilibrium (CPE) in larger regions of the field than in water. CPE is the balance of energy released at a photon interaction point and the energy locally deposited by charged-particles. In large fields and ignoring depth-wise contribution and attenuation, a

point on the central axis can be expected to have dose deposition from any electrons released in a disk of radius R about the central axis, thus balancing the range R of electrons released at the point by photon interactions. However, if the range of released electrons is larger than the field radius, this balance is broken, thereby reducing the dose deposited to the central point. This effect is also ignored with RAT, making its dose calculation in heterogeneous regions like the lung extremely inaccurate.

2.4.2 Monte Carlo

Monte Carlo (MC) methods have been around for almost 70 years, and have been used in diverse areas of science and finance. The core principle of Monte Carlo (MC) methods is the random sampling of events repeated over enough times such that the average outcome of these events can be used to predict a real scenario. In MC simulation of radiation physics, particles are "transported" by calculating the distance to their next interaction. As the interactions are probabilistic, the distance is sampled from a random number and calculated using the total cross section of the particle in the medium. The relative cross section of each interaction is then used to randomly choose the type of interaction which occurs. The simulation is then updated according to the effects of the interaction: the energy and momentum of the initial particle is randomly sampled from known distributions of the given interaction and other particles are created if needed (e.g. release of electrons). This transport process is repeated until all particles have either exit the volume of interest or transferred all their energy. For computational efficiency, it is often the case that a threshold is set such that particles with energies below the threshold are assumed to deposit all their energy locally. The simulation itself is repeated over millions (or more) of initial particles. The results derived from such a simulation follow Poisson statistics such that their relative statistical uncertainty (Type-A) decrease with the square root of the number of particles traversing the region. The latter is proportional to the number of initial particles generated, or "histories". As such, increasing the number of histories induces a linear increase in computation line while only reducing the uncertainty by a square root factor. Due to this reason, MC simulations have historically

been known to be computationally expensive.

One of the earliest and most widely used package developed for MC simulations is the National Research Council's Electron Gamma Shower (EGSnrc) [5] which is a successor of the EGS4 code [6]. Starting out development of EGS at the Stanford Linear Accelerator Center in the 1970's, EGSnrc handles the transport of photons, electrons and positrons over a kinetic energy range of 1 keV to 10 GeV. With the contribution of academic groups, multiple user codes have been available on EGSnrc to create simulations in particular geometries or scenarios, while usually relying on EGSnrc for the actual particle physics.

BEAMnrc

BEAMnrc is one such user code, specifically built to simulate particle transport in linear accelerator heads. A linac model, or beam model, in BEAMnrc typically starts with an electron source, representing the accelerated electrons that impinge the target. Multiple source types are available for the user to model their desired distribution. For conventional linacs, an elliptic source with a Gaussian spread is commonly used. BEAMnrc provides a large set of "component modules" that are geometry classes used to model each of the component downstream, such as the target, collimators, flattening filters or MLC. The user must input geometrical specifications as well as the material and density of each simulated piece. A phase space source file is a collection of particles with their known energy, momentum and type. A phase space file can be collected at the end of a beam model during a simulation to have a representation of the distribution of particles exiting the linac. The phase space file can then be re-used as an input for other simulations, from which initial particles are sampled. Recently, vendors have also distributed phase space source files of their linac heads, usually downstream of the target. This provides the user the ability to accurately model a vendor's linac without having to know detailed information of components upstream from the phase space's position.

DOSXYZnrc

Another such user code is DOSXYZnrc, which is principally used for scoring the dose in user-defined cartesian phantoms or phantoms created from CT images. The user defines the dimension and position of voxels in which the deposited dose is scored. The density and material of the phantom can be customized. Phantoms of CT images can be automatically generated using the accompanying "ctcreate" code. A variety of sources are also available to model different angles or configurations of the incoming radiation. These sources rely on phase space files to sample particles from. In the case of BEAMnrc, a beam model can be compiled as a shared library such that the data of particles crossing the would-be phase space plane are directly input in the DOSXYZnrc simulation. DOSXYZnrc can thus be used to calculate the dose distribution in patients from their treatment plan if there is a beam model of the linac used.

2.5 Stereotactic Body Radiation Therapy

SBRT began as an extension of stereotactic radiosurgery to extracranial sites. Stereotactic radiosurgery is a technique that has been developed since the 1950's [7] and consists of the treatment of brain tumours with high doses of radiation usually delivered in a single fraction. The delivery of such high doses implied stringent precision requirements, which was mostly fulfilled by the Gamma Knife system. Research on translating this technique to extracranial sites started in the 1990's [8]. In the early 2000's the preliminary results for several SBRT clinical trials gave promising outcomes for lung [9]–[11] and liver treatments [12]–[14]. The ICRU defines SBRT treatments as the delivery of higher dose per fraction than in conventional radiation therapy, over fewer fractions. In the Task Group 101 report of the American Association of Physicists in Medicine [15], only treatments delivered in 1 to 5 fractions were classified as SBRT. Recently, treatments over up to 8-10 fractions have also been commonly included [16].

The radiobiological implications of SBRT differ from those of conventional EBRT mainly due to the high dose delivered per fraction. To have a better understanding on the effect of hypofractionation, let us discuss the mathematical model behind cell killing by ionizing radiation. A commonly used simplistic model of the surviving fraction S of cells subjected to a single dose D of radiation is the linear quadratic model proposed by Fowler [17]:

$$S(D) = e^{-\alpha D - \beta D^2}, \tag{2.13}$$

where α and β are tissue-specific constants. The ratio of α/β differs for different tissue type and is an indication of the tissue response to radiation. Larger α/β ratios are associated with early-responding tissue, such that the surviving fraction S decreases rapidly for small D. Most cancer cells, including NSCLC [18], are accepted to be early-responding tissue with α/β ratios on the order of 10 Gy [19].

The Tumour Control Probability (TCP) can be defined to be the probability of eradicating all tumour cells subjected to a dose D. It can be approximated to be [20]:

$$TCP(D) = e^{-N_0 S(D)}, \tag{2.14}$$

where N_0 is the initial number of tumour cells. Plugging the form of $S(D)$ in equation 2.13, we find that the TCP has a sigmoidal relationship with dose, as depicted in Fig.2–10.

Equation 2.13 only describes the behavior for a single dose D. In the case of an evenly fractionated dose, such that cells are irradiated with a dose d per fraction over n fractions, equation 2.13 becomes:

$$S(n, d) = (e^{-\alpha d - \beta d^2})^n \tag{2.15}$$

$$= e^{-n(\alpha d + \beta d^2)}. \tag{2.16}$$

Today, a conventional EBRT treatment is fractionated such that doses of $d = 2$ Gy are given per fraction. Therefore, for any given treatment fractionation scheme to achieve the same cellular damage effect as in a 2 Gy per fraction treatment (spread out over n_2 fractions), we

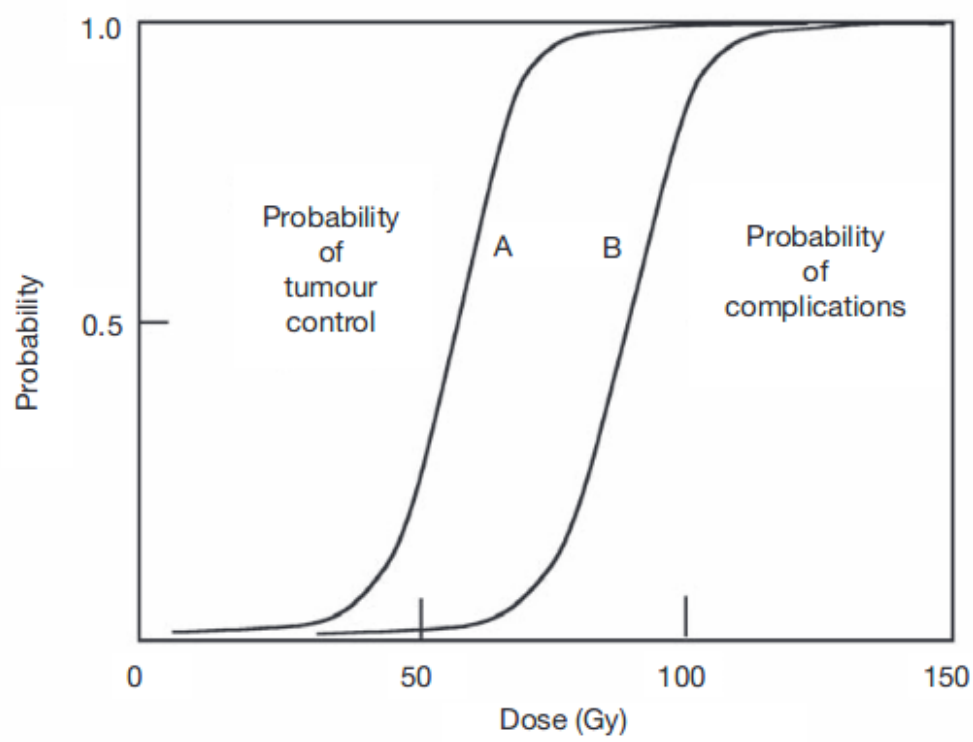

Figure 2–10: Idealistic relationship of TCP (A) and the probability of complications in normal tissue (B) with dose. The TCP curve is characterised by a large gradient region followed by a plateau. In the high dose plateau region, linear increase in dose have limited impact on tumour control. Figure taken from [1]

can equate the survival fraction S in 2.16 due to either fractionation:

$$S(n_2, 2) = S(n, d) \tag{2.17}$$

$$n_2(2\alpha + 4\beta) = n(\alpha d + \beta d^2) \tag{2.18}$$

$$2n_2(\alpha + 2\beta) = nd(\alpha + \beta d) \tag{2.19}$$

$$\frac{2n_2}{\beta}(\alpha/\beta + 2) = \frac{nd}{\beta}(\alpha/\beta + d) \tag{2.20}$$

$$2n_2 = nd\frac{d + \alpha/\beta}{2 + \alpha/\beta} \tag{2.21}$$

$$\text{EQD2} = D\frac{d + \alpha/\beta}{2 + \alpha/\beta}, \tag{2.22}$$

where Equivalent Dose in 2 Gy fractions (EQD2) is the total dose in 2 Gy fractions that is equivalent to a total dose $D = nd$ given in d Gy fractions.

Rearranging equation 2.16 by using $D = nd$:

$$S(n, d) = e^{-D(\alpha+\beta d)}, \tag{2.23}$$

we find that given equal total dose D, the linear quadratic model predicts a more important cellular damage for a larger dose d per fraction. Although the applicability of the linear quadratic model for SBRT remains a subject of debate [4], [21], this is one of the rationale behind using a higher dose per fraction to achieve superior tumor control. Nevertheless, this effect is more prominent for late-responding tissue as it is proportional to β. It thus follows that moving to a hypofractionated treatment would cause more damage to late-responding normal tissue than to early-responding cancer cells. However, thanks to the advance in dose delivery technology such as Intensity Modulate Radiation Therapy (IMRT) and improved image-guidance (e.g. CyberKnife), dose distributions can be made much more conformal to the tumour. As much higher dose can be delivered to the tumour relative to organs at risk, the predicted increase in cellular damage to late-responding tissue can be mitigated while obtaining a superior tumor control [4].

REFERENCES

[1] *Radiation Oncology Physics*, ser. Non-serial Publications. Vienna: INTERNATIONAL ATOMIC ENERGY AGENCY, 2005, ISBN: 92-0-107304-6.

[2] M. Berger, J. Hubbell, S. Seltzer, *et al.* (2010). Xcom: Photon cross section database (version 1.5), [Online]. Available: http://physics.nist.gov/xcom (visited on 07/08/2019).

[3] P. R. Almond, P. J. Biggs, B. M. Coursey, *et al.*, "Aapm's tg-51 protocol for clinical reference dosimetry of high-energy photon and electron beams," *Medical Physics*, vol. 26, no. 9, pp. 1847–1870, 1999. DOI: 10.1118/1.598691.

[4] "Report 91," *Journal of the International Commission on Radiation Units and Measurements*, vol. 14, no. 2, pp. 1–160, Jul. 2017, ISSN: 1473-6691. DOI: 10.1093/jicru/ndx017.

[5] I. Kawrakow and D. W.O. Rogers, "The egsnrc code system: Monte carlo simulation of electron and photon transport," Jan. 2000.

[6] W. Nelson, H. Hirayama, and D. Rogers, "Egs4 code system," Tech. Rep., Dec. 1985.

[7] Y. Nagata, "Introduction and history of stereotactic body radiation therapy (sbrt)," in *Stereotactic Body Radiation Therapy: Principles and Practices*, Y. Nagata, Ed. Tokyo: Springer Japan, 2015, pp. 3–8, ISBN: 978-4-431-54883-6. DOI: 10.1007/978-4-431-54883-6_1.

[8] R. Timmerman, L. Papiez, and M. Suntharalingam, "Extracranial stereotactic radiation delivery: Expansion of technology beyond the brain," *Technology in Cancer Research & Treatment*, vol. 2, no. 2, pp. 153–160, 2003, PMID: 12680797. DOI: 10.1177/153303460300200212.

[9] R. I. Whyte, R. Crownover, M. J. Murphy, *et al.*, "Stereotactic radiosurgery for lung tumors: Preliminary report of a phase i trial," *The Annals of Thoracic Surgery*, vol. 75, no. 4, pp. 1097–1101, 2003, ISSN: 0003-4975. DOI: https://doi.org/10.1016/S0003-4975(02)04681-7.

[10] H. Hof, K. K. Herfarth, M. Münter, *et al.*, "Stereotactic single-dose radiotherapy of stage i non-small-cell lung cancer (nsclc)," *International Journal of Radiation Oncology*Biology*Physics*, vol. 56, no. 2, pp. 335–341, 2003, ISSN: 0360-3016. DOI: https://doi.org/10.1016/S0360-3016(02)04504-2.

[11] Y. Nagata, K. Takayama, Y. Matsuo, *et al.*, "Clinical outcomes of a phase i/ii study of 48 gy of stereotactic body radiotherapy in 4 fractions for primary lung cancer using a stereotactic body frame," *International Journal of Radiation Oncology*Biology*Physics*, vol. 63, no. 5, pp. 1427–1431, 2005, ISSN: 0360-3016. DOI: https://doi.org/10.1016/j.ijrobp.2005.05.034.

[12] K. K. Herfarth, J. Debus, F. Lohr, *et al.*, "Stereotactic single-dose radiation therapy of liver tumors: Results of a phase i/ii trial," *Journal of Clinical Oncology*, vol. 19, no. 1, pp. 164–170, 2001, PMID: 11134209. DOI: 10.1200/JCO.2001.19.1.164.

[13] B. D. Kavanagh, T. E. Schefter, H. R. Cardenes, *et al.*, "Interim analysis of a prospective phase i/ii trial of sbrt for liver metastases," *Acta Oncologica*, vol. 45, no. 7, pp. 848–855, 2006. DOI: 10.1080/02841860600904870.

[14] W. Rule, R. Timmerman, L. Tong, *et al.*, "Phase i dose-escalation study of stereotactic body radiotherapy in patients with hepatic metastases," *Annals of Surgical Oncology*, vol. 18, no. 4, pp. 1081–1087, Apr. 2011, ISSN: 1534-4681. DOI: 10.1245/s10434-010-1405-5.

[15] S. H. Benedict, K. M. Yenice, D. Followill, *et al.*, "Stereotactic body radiation therapy: The report of aapm task group 101," *Medical Physics*, vol. 37, no. 8, pp. 4078–4101, 2010. DOI: 10.1118/1.3438081.

[16] M. Guckenberger, N. Andratschke, H. Alheit, *et al.*, "Definition of stereotactic body radiotherapy," *Strahlentherapie und Onkologie*, vol. 190, no. 1, pp. 26–33, Jan. 2014. DOI: 10.1007/s00066-013-0450-y.

[17] J. F. Fowler, "The linear-quadratic formula and progress in fractionated radiotherapy," *The British Journal of Radiology*, vol. 62, no. 740, pp. 679–694, 1989, PMID: 2670032. DOI: 10.1259/0007-1285-62-740-679.

[18] A. Chi, S. Wen, Z. Liao, *et al.*, "What would be the most appropriate α/β ratio in the setting of stereotactic body radiation therapy for early stage non-small cell lung cancer," *BioMed Research International*, vol. 2013, pp. 1–8, 2013. DOI: 10.1155/2013/391021.

[19] E. J. Hall and (. Giaccia Amato J., *Radiobiology for the radiologist*, English, Seventh edition. Philadelphia, PA : Wolters Kluwer Health/Lippincott Williams & Wilkins, 2012, ISBN: 9781608311934.

[20] T. R. Munro and C. W. Gilbert, "The relation between tumour lethal doses and the radiosensitivity of tumour cells," *The British Journal of Radiology*, vol. 34, no. 400, pp. 246–251, 1961, PMID: 13726846. DOI: 10.1259/0007-1285-34-400-246.

[21] J. M. Brown, D. J. Carlson, and D. J. Brenner, "The tumor radiobiology of srs and sbrt: Are more than the 5 rs involved?" *International Journal of Radiation Oncology*Biology*Physics*, vol. 88, no. 2, pp. 254–262, 2014, ISSN: 0360-3016. DOI: https://doi.org/10.1016/j.ijrobp.2013.07.022.

CHAPTER 3
Large-scale dosimetric assessment of Monte Carlo recalculated doses for lung robotic stereotactic body radiation therapy

Veng Jean Heng, Marc-André Renaud, Robert Doucet, André Diamant, Houda Bahig and Jan Seuntjens

3.1 Abstract

Owing to its short computation time and simplicity, the Ray-Tracing algorithm (RAT) has long been used to calculate dose distributions for the CyberKnife system. However, it is known that RAT fails to fully account for tissue heterogeneity and is therefore inaccurate in the lung. The aim of this study is to make a dosimetric assessment of 219 non-small cell lung cancer CyberKnife plans by recalculating their dose distributions using an independent Monte Carlo (MC) method. As expected, target coverage was found to be significantly compromised when considering MC doses as only 27% of plans were found to comply to their prescription doses. For the majority of the cases, normal tissue dose limits were respected with the worst non-compliance rate (7%) observed in the rib. Comparison of RAT and recalculated-MC doses confirms the overestimation of RAT doses observed in previous studies. An inverse correlation between the RAT/MC dose ratio and the target size is also found to be statistically significant ($p < 10^{-4}$), consistent with other studies. In addition, this study has demonstrated the inaccuracy and variability in target coverage incurred from dose calculations using RAT without heterogeneity corrections. Despite significant deterioration in target coverage, no correlation was observed between the compliance of the prescription $D_{95\%}$ and loco-regional control rates. On average, no clinically relevant differences were observed between MC-calculated dose-to-water and dose-to-medium for all tissues investigated ($\leq$1%).

3.2 Introduction

For medically inoperable non-small cell lung cancer (NSCLC) patients, stereotactic body radiation therapy (SBRT) has been demonstrated to be a promising treatment alternative. Indeed, as reported in multiple studies [1]–[3], the 3-year local control rate of early-stage NSCLC patients treated with SBRT is over 90%. Specifically, increased dose prescribed to the tumor has been shown to be strongly correlated to better local control and survival rates [4]. For adequate lung cancer treatment, it is therefore imperative to deliver sufficient and accurate doses to the tumor.

With its image-guidance kit, the CyberKnife (Accuray Inc., Sunnyvale, CA) system is particularly adapted for lung SBRT, where breathing motion may compromise the accuracy of dose delivery. Dose calculation of CyberKnife treatment plans are carried out on the MultiPlan (v5.3.0) system. The first dose calculation method implemented in MultiPlan was the Ray-Tracing (RAT) algorithm. Ray-Tracing calculations rely on tabulated measurements of the beam's profile, depth doses and output factors in homogeneous water phantoms. To account for variation in tissue density, RAT scales in-patient depths by using the effective path length. The latter is calculated as the ratio of the electronic density of traversed voxels to the electron density of water (unit density). It is well known that this method fails to account for differences in the beam's scatter component and is therefore inaccurate in regions of heterogeneity [5]–[7]. This is because RAT, like other factor-based algorithms, does not correct for differences in lateral scatter in an inhomogeneous medium. For this reason, the International Commission on Radiation Units and Measurements (ICRU) has recommended the use of type-b model-based algorithms which do model lateral electron transport (ICRU 91)[8]. A fast Monte Carlo (MC) type-b dose calculation algorithm [9], [10] has been available on MultiPlan as of v2.1 and after. Although MC algorithms are considered the gold standard in terms of dose calculation accuracy, the MC algorithm used by MultiPlan makes use of a few approximations to minimize computational time. MultiPlan's MC algorithm transports photons in medium using the medium's mean free path. The latter is determined

from the mass density of the voxel. Electron tracks are pre-generated in water and have their step length scaled based on the voxel's density. The MC algorithm of MultiPlan therefore effectively outputs dose to varying density of water.

Various studies [11]–[15] have compared dose distributions of lung plans as calculated by RAT and fast MC. All studies have reported RAT to overestimate target doses, with maximum doses being overestimated by up to a factor of 1.63 [11]. Braunstein et al. [15] found that the ratio of RAT to MC doses was inversely correlated to target size and its overlap with soft-tissue.

Past lung SBRT clinical trial protocols such as Radiation Therapy Oncology Group (RTOG) 0236 and RTOG 0618 [1], [3], dictated stringent dosimetric constraints despite requiring plans to be planned without heterogeneity corrections (HC). In this case where all tissues are treated as unit density water, neither RAT nor MC would accurately estimate the physically delivered dose in the lung region. In this study, the dosimetric adequacy of a large set of NSCLC patient plans will be re-assessed based on dose distributions recalculated using an independent MC method with HC.

3.3 Materials and Methods

3.3.1 EGSnrc model

A Monte Carlo (MC) model of the CyberKnife G4 system was built on the BEAMnrc user code of the EGSnrc package [16]. A monoenergetic electron beam source of energy E was simulated normally incident on the target. The radial distribution of the electron beam was Gaussian with spot size σ. All components downstream from the target, which include the primary collimator, a lead electron filter, the patient plane shield and the 12 fixed conic collimators have their geometry and position initially modelled from technical drawings. The electron beam parameters were initially set to be similar to reported literature values [10], [17]. Measurements performed during the commissioning of the CyberKnife G4 system at the Centre hospitalier de l'Université de Montréal served as a baseline to tune

the electron beam parameters and dimension of the component modules. All measurements were taken at 80 cm source-axis distance (SAD) in a water tank using a PTW60012 diode. An open-field profile, for which no fixed conic collimator was attached to the CyberKnife head, was taken at 2.5 cm depth. Tissue-Maximum Ratio (TMR) and profile measurements were made for all fixed collimators. Profiles were taken at the depth of maximum dose $d_{\max}$ = 1.5 cm. An open-field profile was firstly calculated using the MC model by irradiating a 28×28×10 cm^3 water phantom on the DOSXYZnrc user code in the same conditions as the measurements. For all validation simulations, doses were scored in cubic voxels of 1 mm^3 and sufficient histories were used to obtain a Type A uncertainty of less than 1% in voxels receiving at least 20% of the maximum dose scored. Standard cut-off energies were used, i.e., for electrons ECUT = 0.7 MeV (total energy) and for photons PCUT = 0.01 MeV. The spot size σ of the electron beam, the opening radii of the primary collimator and of the patient plane shield were iteratively adjusted to empirically match the measured profile. The TMR and radial profile of the 60 mm fixed collimator was then calculated from MC simulation in measurement conditions. For TMR(z) simulations, the water phantom had dimensions of 10×10×(z+10) cm^3 where z is the depth at which TMR is evaluated for that given simulation. The energy E of the electron beam was adjusted to match the simulated and measured TMRs. Similarly, the opening radii of the fixed collimator was tuned according to differences in radial profiles. This iterative process was repeated for the profiles of all other fixed secondary collimators. The dose scored in the voxel on the central axis at $d_{\max}$ was used to calculate the output factor for each collimator. Commissioning measurements of output factors were also taken with the PTW60012 diode at $d_{\max}$ as the ratios of the raw detector reading for each collimator size to the reading for the 60 mm collimator. These ratios were corrected for the field size dependency of the detector's response by using the TRS-483 output correction factors interpolated based on the full width at half maximum of the radial profile at the measurement depth[18].

Table 3–1: Patient set characteristics

Fractionation scheme (Gy/fx)	Number of patients planned with: RAT without HC	RAT with HC	MC with HC
40/3	0	0	1
40/5	2	0	0
48/4	1	0	0
50/4	20	0	0
50/5	29	1	1
54/5	0	0	1
60/3	109	10	12
60/5	16	8	6
60/8	1	0	1

3.3.2 Patient set

From July 2009 to February 2015, 219 non-small cell lung cancer (NSCLC) stage I patients were treated with stereotactic body radiation therapy (SBRT) on the CyberKnife system using circular collimators. All patients were either medically inoperable or refused surgery. Only patients with a single lesion were analysed in this study. Patients were CT scanned in a supine position on a 512×512 grid with 1 mm slice thickness. Prescription doses varied from 40-60 Gy and were delivered in 3-8 fractions (Table.3–1). The gross tumor volume (GTV) was contoured on CT images and the planning target volume (PTV) is defined as a 5 mm extension to the GTV. The prescription isodose surface was chosen such that at least 95% of the PTV was covered by the prescription dose, although higher priority was given to respecting maximum doses to organs at risk (OAR). Planning was done on Accuray's MultiPlan treatment planning system (TPS) (versions 3.5 and 4.5), with 197 patient doses calculated by RAT and 22 by MC. TPS MC doses were calculated with a Type A (k=1) uncertainty of either 1 or 2%. Out of the 197 RAT plans, 178 of those were planned without HC: tissue above -800 Hounsfield unit (HU) were set to water with 1 g/cm^3 density. Note that CT numbers in this paper are defined in units of HU which differ from MultiPlan's CT numbers by an intercept shift of -1000 (e.g., -800 HU = 200 MultiPlan CT number). Patients before November 2013 were treated on the G4 model of the CyberKnife, while the remaining

ones were treated on the VSI model. No significant dosimetric difference between the two CyberKnife models had been observed in their commissioning measurements. Patients were followed-up for loco-regional progression 1-3 months after their last treatment and every 3-6 months thereafter.

3.3.3 Plan recalculation and analysis

All patient plans were recalculated with the BEAMnrc MC model on DOSXYZnrc, while keeping all beam parameters (node position, beam weights, etc.) the same. This was done using source 21, developed by Lobo and Popescu **Lobo˙2010** The same MC model was used to recalculate both G4 and VSI plans. In-plane voxel dimensions were chosen to be double the CT pixel spacing to reduce computation time while the axial voxel dimension was kept equal to the CT slice thickness. Sufficient histories were ran such that the statistical uncertainty in the 20 voxels receiving the highest dose is less than 1%. To this effect, history counts were scaled by the squared diameter of the collimator used. Dose distributions output by DOSXYZnrc were converted to absolute absorbed dose by multiplying all voxel doses by the total monitor unit (MU) delivered with the given collimator and a MC-to-reference dose conversion factor N:

$$D_{\text{absolute}}(\text{Gy}) = d_{\text{MC}}(\text{Gy}_{MC})N(\frac{\text{Gy}}{\text{Gy}_{MC}\text{MU}})\text{MU}, \tag{3.1}$$

where the conversion factor N was calculated by dividing the machine's calibration factor of 0.01 Gy/MU by the dose per incident particle $d_{\text{MC}}(\text{ref})$ scored to high precision (<0.1%) by DOSXYZnrc in a 1 mm^3 voxel under reference condition. $d_{\text{MC}}(\text{ref})$ was calculated at $d_{\max}$ and SAD = 80 cm with the 60 mm collimator. Dose-to-water was calculated by setting all tissues within the body contour to be water with varying mass density determined by a CT-density curve. Regions outside the body contour had their density overridden to air density (0.0012 g/cc) to avoid beam attenuation due to CT artifact.

There has been considerable debate on the relevancy of reporting dose-to-medium against dose-to-water [19]. It was chosen to report the latter in this study as previous clinical dosimetric expertise in CyberKnife lung treatments had been based on doses-to-water calculated by the RAT algorithm. Andreo [20] had reported analytical differences between these two calculation approaches to be less than 1% in soft-tissue and lung. Only in bone has the difference between these two approaches been observed to be clinically significant [20]–[22]. Nevertheless, all patient plans were also recalculated for their dose-to-medium by using the following medium within the body contour: ICRUTISSUE700ICRU, LUNG700ICRU and ICRPBONE700ICRU. The medium of a voxel is assigned based on the voxel's CT number range. Dosimetric differences between these two approaches for MC-calculated lung plans are reported.

The following dosimetric characteristics of the PTV were analysed: the dose $D_{95\%}$ delivered to 95% of the PTV, the near-maximum dose $D_{2\%}$, near-minimum dose $D_{98\%}$ and mean PTV dose D_{mean}. PTV doses were converted to equivalent dose in 2 Gy fractions (EQD2) using the linear quadratic model [23] to account for differences in fractionation scheme (Table 3–1) with $\alpha/\beta = 10$ Gy. The homogeneity index (HI) and the conformity index (CI) were also calculated as:

$$HI = \frac{D_{2\%} - D_{98\%}}{D_{50\%}}, \tag{3.2}$$

$$CI = V_{\text{PD}}/V_{\text{PTV}}, \tag{3.3}$$

where $D_{2\%}$, $D_{98\%}$ and $D_{50\%}$ are evaluated in the PTV, and where V_{PD} is the volume receiving at least the prescription dose and V_{PTV} is the volume of the PTV. Volumes of structures in this study were calculated by summing the volume of dose voxels within the structure's contour. The difference in dose distribution between the one given by the TPS and the MC recalculation was estimated by a scatter plot of every plan's EGSnrc-calculated D_{mean} against TPS-calculated D_{mean}. For RAT plans, the correlation between the ratio of D_{mean} as

calculated by these two previous methods and the volume of the PTV was assessed by calculating the Spearman rank correlation. The correlation between loco-regional control rates and dose coverage was tested by performing a Kaplan-Meier analysis of the loco-regional progression-free survival. Patients were split in two groups according to their compliance of their MC-recalculated PTV dose coverage to their prescription dose ($D_{95\%} \geq$ prescription dose). A log-rank test was used to determine the difference in survival between the two patient groups. Statistical significance in this study is defined for $p < 0.05$. In a separate analysis, the cohort was split by thresholding the target coverage dose $D_{95\%}$ by an absolute EQD2. The above-mentioned Kaplan-Meier analysis was repeated for the two resulting subgroups. If the latter were found to be significantly different by the log-rank test, a hazard ratio and its 95% confidence interval (95%CI) were computed from a univariate Cox proportional hazards regression model.

Near-maximum $D_{2\%}$ dose were compiled for the following OAR: heart (75%), spinal cord (97%), brachial plexus (28%), esophagus (84%), trachea and large bronchus (68%), segmental bronchi (50%), great vessels (43%) and ribs (100%). Not all OARs were available for all patients. The percentages quoted above in brackets represent the fraction of patients for which the OAR was contoured. If 2% of the OAR volume was smaller than 0.03 cm^3, the near-maximum dose to at least 0.03 cm^3 was instead taken as recommended in the Report 91 of the ICRU [8]. This occurred in only 42 cases (3.5%) across all OAR, with 41 of them involving the bronchus. The fraction V_{20Gy} of the whole (right and left) lung volume (minus PTV) receiving at least 20 Gy was also calculated. These calculated normal tissue doses were compared to the dose limits that were used when planning for these patients.

3.4 Results

3.4.1 EGSnrc model validation

The radial profiles at d_{max} calculated by the MC model is plotted in Fig.3–1 for all 12 collimator sizes. The off-center ratio (OCR) is normalized by the dose on the central-axis.

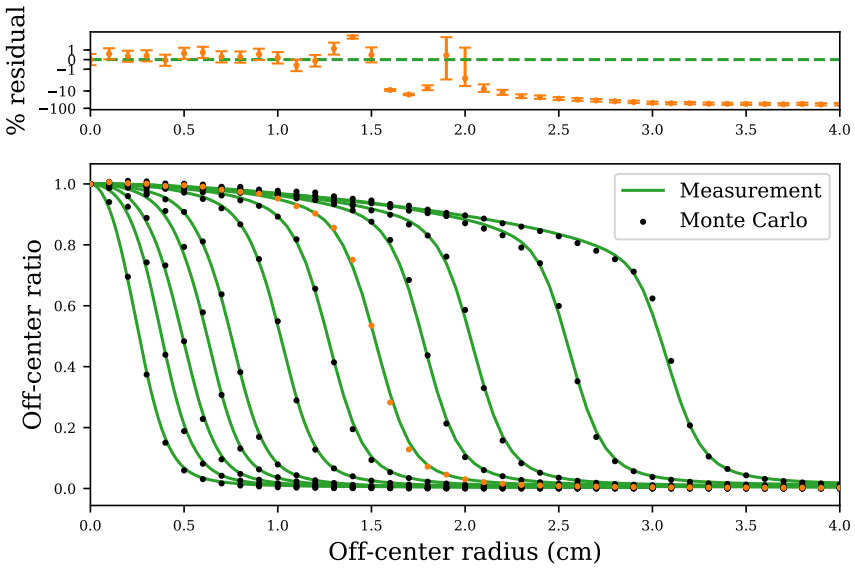

Figure 3–1: OCR for all 12 collimators (5, 7.5, 10, 12.5, 15, 20, 25, 30, 35, 40, 50 and 60 mm diameter). Although an offset is present in the shoulder of the largest collimator profile (60 mm), that collimator was not used in CyberKnife treatment plans. For clarity, the local residuals are only plotted for the 30 mm collimator (orange), which was the the most often used collimator in this study.

Despite a slight offset in the shoulder of the 60 mm collimator profile, this set of primary collimator opening and $\sigma = 0.85$ mm were chosen as they provided the best agreement for the other collimators. The smallest collimator (5 mm) required a different spot size $\sigma = 0.95$ mm for a better agreement with measured output factors. Neither of these two collimators (60 mm and 5 mm) were used in the patient plans of this study. From the residuals, for all collimators, the out-of-field dose is underestimated by the MC model. The latter is however negligible for patient plan recalculations as its absolute contribution to the delivered dose is less than the statistical uncertainty in the target dose. Monte Carlo-calculated output factors were found to match measurements to within better than 1% for all collimators (Fig.3–3). This ensures that the systematic dose offset introduced when recalculating plans of different collimator sizes is smaller than the statistical uncertainty in Monte Carlo doses. A monoenergetic electron beam source of energy $E = 7.0$ MeV was found to provide the best agreement between calculated and measured TMRs (Fig.3–2).

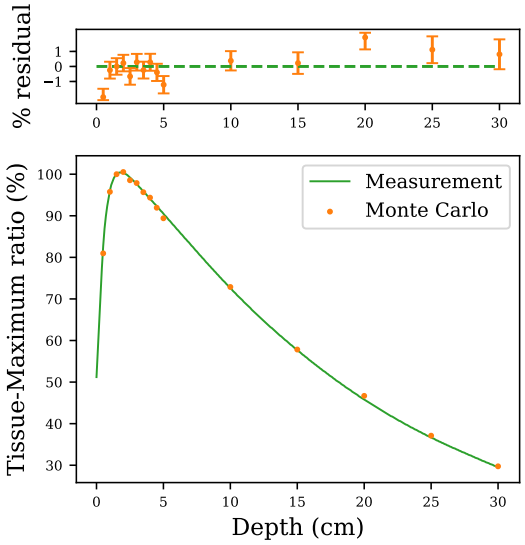

Figure 3–2: TMR for the 60 mm collimator up to 30 cm depth. Type A uncertainties of Monte Carlo doses are shown in the local residual plot.

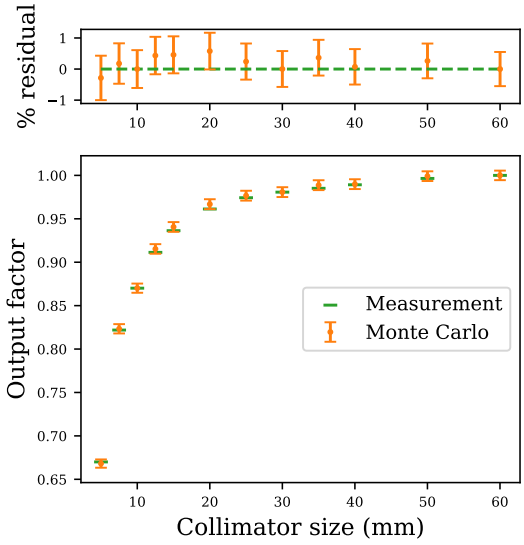

Figure 3–3: Output factor for all collimator sizes. Agreement between MC calculation and measurement is observed within 1%.

3.4.2 Dosimetric characteristics

Patient plans were separated into three subsets according to the method with which the planning dose was calculated. The plot in Fig.3–4 shows the distribution of the mean recalculated PTV dose against the TPS's calculated dose, for all subsets. Firstly, all MC-planned mean PTV doses lie near the line of identity, thus supporting an agreement between the two MC models. The ratio of TPS MC to EGSnrc MC-calculated D_{mean} has a median value of 1.02 (0.96-1.04). Secondly, as expected, the majority of RAT plans have their PTV dose overestimated by the TPS. However, the extent of this error is not uniform for all plans. Indeed, the ratio of RAT to EGSnrc MC PTV mean dose was found to have a median value of 1.08 with a range of (0.78-1.72). For RAT plans that were calculated using HC, this ratio was found to be always positive with a median of 1.29 (1.13-1.44). However, 32% of RAT plans that did not use HC had a higher recalculated dose. These patients were found to have a higher mean CT number (-700 HU) inside their lung contour (minus PTV) than the remaining 68% (-779 HU). For all RAT plans, an inverse correlation between the dose ratio of RAT to EGSnrc-calculated D_{mean} and the PTV volume is observed in Fig.3–5 with

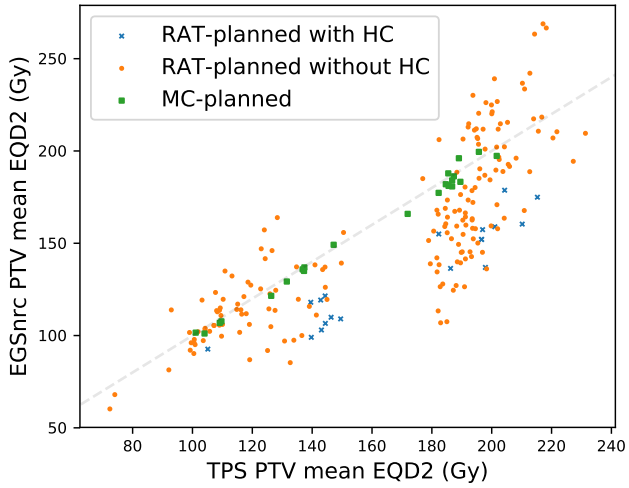

Figure 3–4: Scatter plot of mean dose to the PTV as recalculated by EGSnrc against the TPS dose. Plans were separated according to the method with which the doses were calculated. Points close to the line of identity have similar TPS and EGSnrc recalculated mean PTV dose.

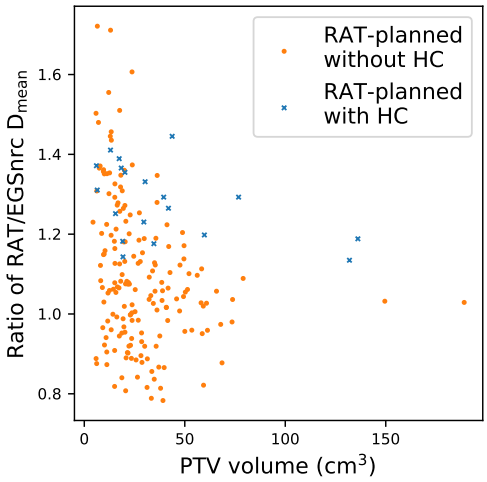

Figure 3–5: Scatter plot of the ratio of RAT-calculated to EGSnrc-calculated D_{mean} as a function of PTV volume. A Spearman correlation of -0.29 ($p < 10^{-4}$) suggests an inverse correlation between the RAT/EGSnrc PTV dose ratio and the PTV's size.

a Spearman correlation coefficient of -0.29 ($p < 10^{-4}$).

The PTV dose characteristics in all patients of the cohort is represented in the boxplot in Fig.3–6. The EQD2 shown are calculated from the EGSnrc MC recalculated dose distribution. Only 27% (60) of the plans were found to have their recalculated dose satisfy the planning PTV coverage goal ($D_{95\%} \geq$ prescription dose), as opposed to 70% when analysing the TPS dose. Both the HI and CI were found to be highly diverse with median (range) values of 0.66 (0.28-1.22) and 0.93 (0.06-2.31) respectively. The loco-regional progression-free survival curves in Fig.3–7a found no statistically significant differences between the loco-regional control rates when separating patients according the compliance of $D_{95\%}$ to their respective prescription dose. However, when patients are separated by a threshold EQD2 $D_{95\%} \geq$119 Gy, their loco-regional progression-free survival curves were found to be statistically distinct using a log-rank test with a p-value of 0.027 (Fig.3–7b). The hazard ratio

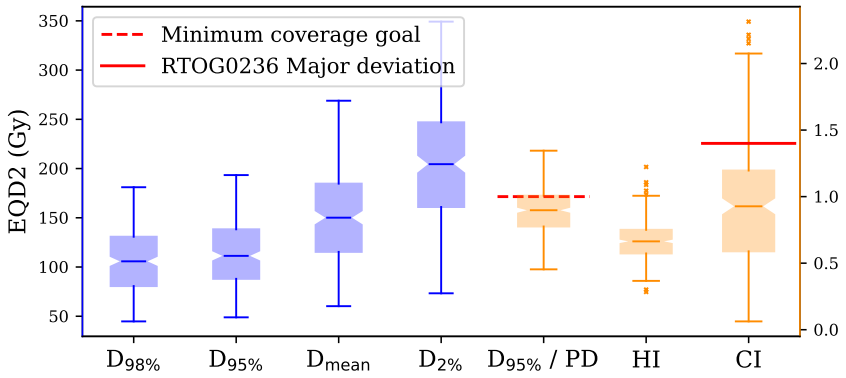

Figure 3–6: PTV coverage parameters for all 219 patient plans, based on MC-recalculated dose distributions. The target coverage goal of $D_{95\%} \geq$ Prescription Dose (PD) is only achieved in 27% of the plans when assessed on MC doses.

was calculated to be 3.28 (95%CI:1.07-9.97). The threshold EQD2 of 119 Gy was chosen as it resulted in the minimum p-value for the log-rank test. For reference, this threshold corresponds to a dose prescription of 52 Gy in 3 fractions.

The near-maximum doses delivered to OAR as calculated by EGSnrc MC are also shown in Fig.3–8. Although planning dose limits applied to the maximum dose to any voxel, $D_{2\%}$ was calculated in this study as single-voxel doses are not meaningful in MC calculations due to its inherent statistical uncertainty. The rib is the OAR with the lowest compliance rate (93%) to the normal tissue dose limits followed by the segmental bronchi (94%), the brachial plexus (95%) and the esophagus (99%). Maximum doses to all other organs-at-risk comply to the limits for all plans.

3.4.3 Dose-to-medium

The above-mentioned OAR doses and the PTV's $D_{95\%}$ were recalculated using their plan's dose-to-medium dose distribution. The ratio of these metrics are shown in Fig.3–9. The medium tissue of the heart, brachial plexus, esophagus and great vessels being assigned to soft-tissue in the MC simulation have a smaller dose-to-medium than their dose-to-water counterpart. This is in agreement with the calculated ratio of 0.996 by Andreo

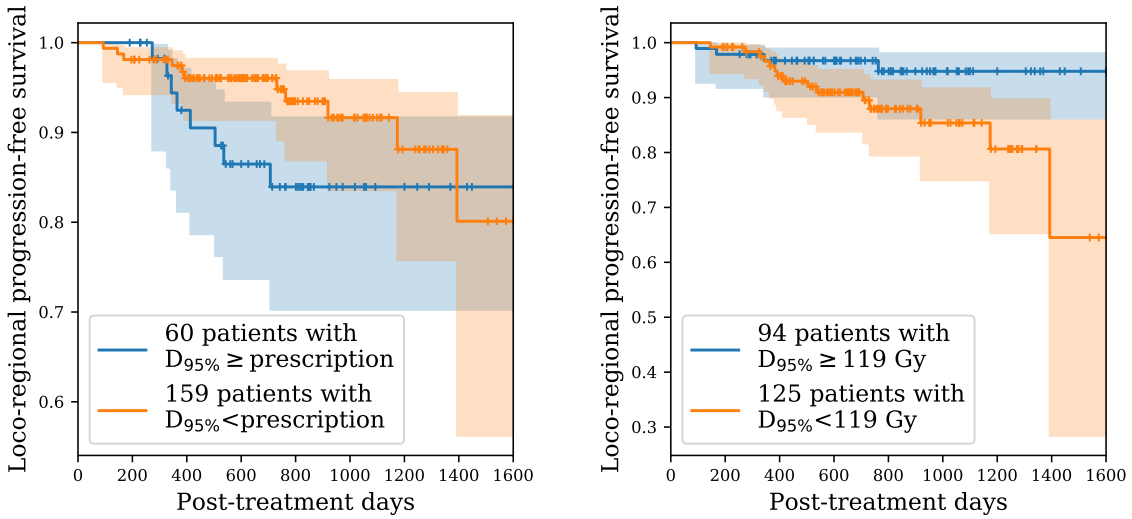

(a) Separated by compliance to prescription dose. $p = 0.15$

(b) Separated by a threshold EQD2 of 119 Gy. Hazard Ratio = 3.28 (95%CI: 1.07-9.97), $p = 0.027$

Figure 3–7: Loco-regional progression-free survival rate as a function of post-treatment days. Notches in the plot represent censoring due to lack of further of follow-ups. Shaded areas represent the 95% confidence band. The p-value of a log-rank test between the two curves is given.

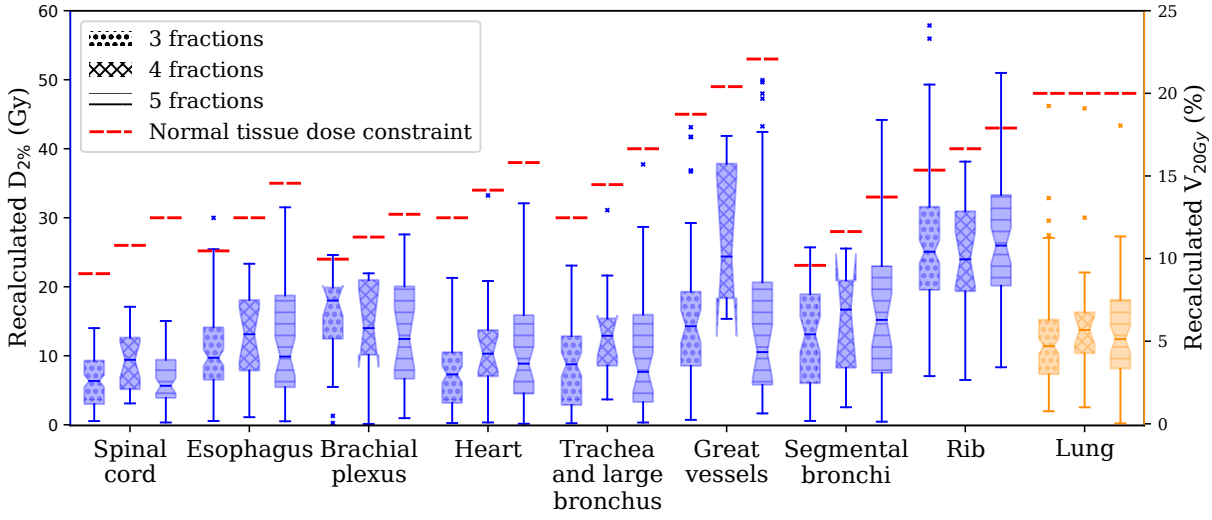

Figure 3–8: Near-maximum $D_{2\%}$ doses delivered to OAR as recalculated by EGSnrc MC. For the lung, it is the fraction V_{20Gy} of lung volume receiving at least 20 Gy that is reported. Plans were separated according to their number of fractions to reflect the different dose limits of each fractionation scheme. Outliers are represented by crosses. The dose line corresponding to the normal tissue dose limits used for planning are drawn. Two patients had treatments delivered in 8 fractions and were not included in this plot.

[20] for soft-tissue. Although the spinal cord is also assigned to soft-tissue, it is surrounded by bone. This makes most of its volume fall within the bone/soft-tissue interface region, which does not have a uniform dose-to-medium to dose-to-water ratio [22]. Although bone is known to be overestimated by dose-to-water by 4∼6% for 6 MV beams [21], [22], the median D_{medium}/D_{water} ratio for the rib is not as different from unity (0.99). That is because the rib contour in the large majority of patients include surrounding soft-tissue which constitute the majority of its voxels. For some patients, only rib bones are featured in the contour. These patients thus have much smaller dose-to-medium to dose-to-water ratio and are then becoming outliers in the boxplot. Similarly, for great vessels, low D_{medium}/D_{water} outliers correspond to patients which had CT images featuring contrast agents. As such for these patients, most vessel voxels had artificially higher CT number and were assigned to be bone as a result. The slightly larger than unity ratio observed for the lung agrees with the slightly larger than 1 stopping power ratio of LUNG700ICRU calculated at this energy [24]. Although the PTV's medium is mostly assigned to soft-tissue, some patients with small tumors (eg. outliers in Fig.3–9) have a significant proportion of lung tissue within their PTV. Overall, the median difference produced from using dose-to-medium instead of dose-to-water is at most 1% for all investigated organs and target.

3.5 Discussion

Recalculated MC doses analysed in this study were obtained from a beam model built with EGSnrc. The beam model was manually fine-tuned to match commissioning measurements of TMR, OCR and output factors. Similarly, these measurements were used by the TPS to commission its own beam model. Therefore, differences between our EGSnrc beam model and the TPS beam model can be estimated from the local residuals given in Fig.3–1, 3–2 and 3–3. Although local residuals on the order of 10% and 100% can be observed in the penumbra and out-of-field region respectively, the in-field dose agrees with measurements within 1%. This is demonstrated by the close agreement between mean PTV doses as calculated by the TPS MC and the recalculated MC dose (Fig.3–4). Discrepancies between the

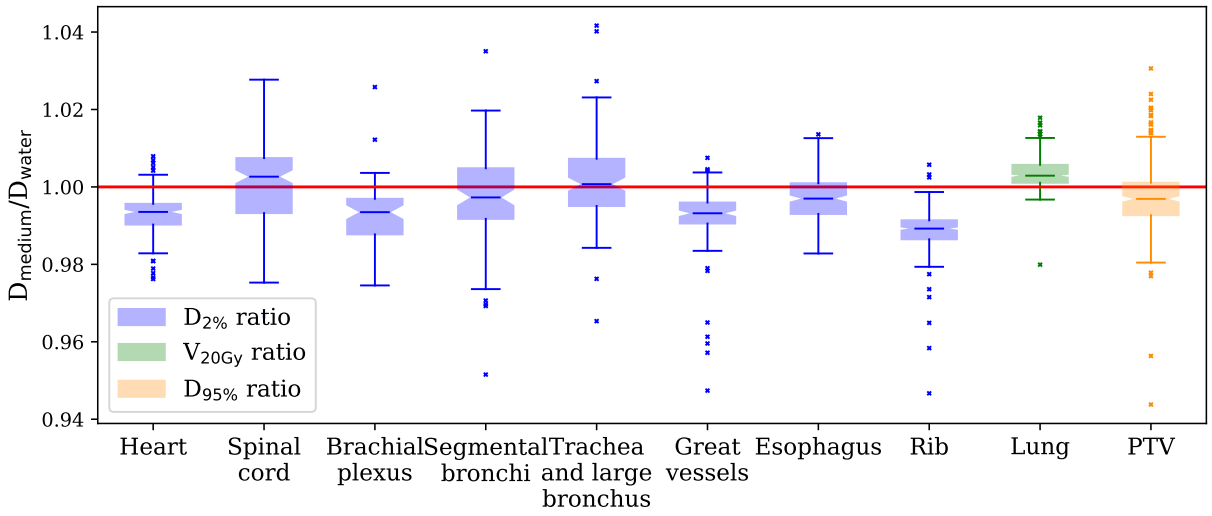

Figure 3–9: Ratios of dosimetric parameters as calculated using dose-to-medium to the same parameters using dose-to-water. Note that for the lung, it is a ratio of volumes and not doses that is shown. For OAR points, only plans where the OAR received $D_{2\%} \geq 4$ Gy, and therefore sufficiently small statistical uncertainty, were plotted. For similar reasons, if 2% of the OAR volume was smaller than 0.03 cm^3, the maximum dose deposited in at least 0.03 cm^3 was instead recorded.

beam models are therefore negligible when compared to the differences observed between RAT with or without HC and MC doses.

The major factor that affects the relative difference between RAT and MC dose is the contribution of miscalculated scatter to the point of interest. The proportion of this scatter contribution depends on the immediately surrounding tissue density. Points located in soft-tissue with near-water density will have their lateral scatter contribution accurately approximated by RAT whereas the dose at points in the middle of the lung or next to high-density bone will be respectively over and underestimated [6]. As tumor densities are close to unity, only points on the extremity of PTVs, which are either near or within lung tissue, are generally overestimated by RAT. Indeed, for all plans initially calculated by RAT with HC, PTV doses were found to be lower when calculated with EGSnrc MC. Similarly, as large PTVs have a larger proportion of voxels within the near-water density tumor, their mean dose calculated by RAT is closer to the EGSnrc value than for smaller PTVs, as observed in Fig.3–5. This correlation with target size is consistent with past studies [12]. In order to

deliver doses that are similar to previous RAT-based prescription while using type-b algorithms, the method proposed by Lacornerie et al. [25] could be used. The dose should be prescribed to the GTV instead of the PTV as it does not encompass as much low-density lung tissue.

When calculated without HC, doses to the PTV can be underestimated due to over-attenuation of the beams through lung tissue. Indeed, in the case of this study, if the CT number of the lung tissue is above the -800 HU threshold, its density would be erroneously overestimated to 1 g/cm^3. However, the contrary is also true if the lung's CT number is under -800 HU, in which case beams traversing the lung will be under-attenuated and the overestimation of PTV doses by RAT is amplified.

The deviation of dose calculations of lung plans without HC from physically delivered doses are thus highly variable across patients. As was observed in Fig.3–4, if MC doses are assumed to accurately reflect delivered doses, PTV doses calculated without HC are susceptible to both underestimation and overestimation, by factors ranging from 0.78 to 1.72. Planning constraints regarding target coverage enforced in study protocols that mandated the non-usage of HC, such as RTOG0236 and RTOG0618, therefore become inconsequential when considering the disparity between calculated and delivered doses. Based on an analysis by Xiao et al. [26], Timmerman et al. [1] quoted the RTOG 0236 prescription dose of 60 Gy in 3 fractions to be delivered as 54 Gy when taking into account HC. However, the present study shows that no simple uniform conversion factor can be made to estimate actual delivered doses from dose calculations without HC. Such estimate would have to take into account patient-specific parameters such as the lung's mean density, the target's size and position.

Despite these discrepancies, compliance of delivered dose to OAR dose limits was the case for the large majority of plans in this cohort. Indeed, assuming that the TPS dose

adequately complies to the normal tissue dose limits, only RAT plans without HC that had a higher PTV dose when recalculated are susceptible to overdose the OARs. Out of those, only OARs close enough to the target to receive a considerable dose will be at risk of being overdosed. Thus, in most cases, physically delivered doses to OARs do not exceed their imposed limits. On the other hand, target coverage for lung patients can be severely compromised if the dose is calculated using RAT, with or without HC. In our cohort, when re-assessed using the EGSnrc MC dose, only 27% of the plans satisfied the prescribed target coverage. Nevertheless, no correlation was found between loco-regional control rates and the target coverage of the prescription dose. However, target coverage with a dose above a threshold was found to be a better indicator of loco-regional control. This supports the generally accepted [4] positive correlation between dose to the target and local control rates. However, although Onishi et al. [4] had found superior local control rates for patients being prescribed biologically effective dose (BED) of more than 100 Gy (=83.3 EQD2 Gy) to the isocenter. In our study, no statistically significant distinction in loco-regional control rates could be found with threshold BED lower than 124.8 Gy (=104 EQD2 Gy).

3.6 Conclusions

The aim of this study was to retrospectively assess the dosimetry of lung CyberKnife plans by recalculating them using an independent, highly accurate MC method. Target coverage parameters were severely worsened in the majority of plans when compared to their original doses, whereas OAR dose limits were generally respected. Dose distributions originally calculated without HC and using the TPS RAT were observed to have the largest disparity with MC doses. The magnitude of this discrepancy was found to be non-uniform across patients, thus underlining the importance of using MC or advanced type-b algorithms when calculating lung doses. Conclusions regarding the adequacy of prescription doses or target coverage goals obtained from clinical trials requiring no HC should therefore be re-examined.

3.7 Acknowledgements

This work was supported by the CREATE Medical Physics Research Training Network [grant number 432290] of the National Sciences and Engineering Research Council and NSERC RGPIN-2014-06475.

REFERENCES

[1] R. Timmerman, R. Paulus, J. Galvin, *et al.*, "Stereotactic Body Radiation Therapy for Inoperable Early Stage Lung Cancer," *JAMA*, vol. 303, no. 11, pp. 1070–1076, Mar. 2010, ISSN: 0098-7484. DOI: 10.1001/jama.2010.261.

[2] A. Navarro-Martin, S. Aso, J. Cacicedo, *et al.*, "Phase ii trial of sbrt for stage i nsclc: Survival, local control, and lung function at 36 months," *Journal of Thoracic Oncology*, vol. 11, no. 7, pp. 1101–1111, 2016, ISSN: 1556-0864. DOI: https://doi.org/10.1016/j.jtho.2016.03.021.

[3] R. D. Timmerman, R. Paulus, H. I. Pass, *et al.*, "Stereotactic Body Radiation Therapy for Operable Early-Stage Lung Cancer: Findings From the NRG Oncology RTOG 0618 Trial Stereotactic Body Radiation Therapy for Operable Early-Stage Lung Cancer Stereotactic Body Radiation Therapy for Operable Early-Stage Lung Cancer," *JAMA Oncology*, vol. 4, no. 9, pp. 1263–1266, Sep. 2018, ISSN: 2374-2437. DOI: 10.1001/jamaoncol.2018.1251.

[4] H. Onishi, H. Shirato, Y. Nagata, *et al.*, "Hypofractionated stereotactic radiotherapy (hypofxsrt) for stage i non-small cell lung cancer: Updated results of 257 patients in a japanese multi-institutional study," *Journal of Thoracic Oncology*, vol. 2, no. 7, Supplement 3, S94–S100, 2007, ISSN: 1556-0864. DOI: https://doi.org/10.1097/JTO.0b013e318074de34.

[5] C. Ma, J. Li, J. Deng, and J. Fan, "We-c-aud-03: Investigation of fast monte carlo dose calculation for cyberknife srs/srt treatment planning," *Medical Physics*, vol. 34, no. 6Part20, pp. 2589–2590, 2007. DOI: 10.1118/1.2761510.

[6] E. E. Wilcox and G. M. Daskalov, "Accuracy of dose measurements and calculations within and beyond heterogeneous tissues for photon fields smaller than produced by

cyberknife," *Medical Physics*, vol. 35, no. 6Part1, pp. 2259–2266, 2008. DOI: 10.1118/1.2912179.

[7] V. Murali, P. G. Gopalakrishna Kurup, N. Bhuvaneswari, H. Sudahar, and M. Muthukumaran, "Monte carlo and ray tracing algorithms in the cyberknife treatment planning for lung tumours- comparison and validation," *Journal of radiosurgery and SBRT*, vol. 2, no. 2, pp. 85–98, 2013, ISSN: 2156-4639.

[8] "Report 91," *Journal of the International Commission on Radiation Units and Measurements*, vol. 14, no. 2, pp. 1–160, Jul. 2017, ISSN: 1473-6691. DOI: 10.1093/jicru/ndx017.

[9] J. Deng, C.-M. Ma, J. Hai, and R. Nath, "Commissioning 6 mv photon beams of a stereotactic radiosurgery system for monte carlo treatment planning," *Medical Physics*, vol. 30, no. 12, pp. 3124–3134, 2003. DOI: 10.1118/1.1624753.

[10] C.-M. Ma, J. S. Li, J. Deng, and J. Fan, "Implementation of monte carlo dose calculation for CyberKnife treatment planning," *Journal of Physics: Conference Series*, vol. 102, p. 012 016, Feb. 2008. DOI: 10.1088/1742-6596/102/1/012016.

[11] E. E. Wilcox, G. M. Daskalov, H. Lincoln, *et al.*, "Comparison of planned dose distributions calculated by monte carlo and ray-trace algorithms for the treatment of lung tumors with cyberknife: A preliminary study in 33 patients," *International Journal of Radiation Oncology*Biology*Physics*, vol. 77, no. 1, pp. 277–284, 2010, ISSN: 0360-3016. DOI: https://doi.org/10.1016/j.ijrobp.2009.08.001.

[12] N. C. van der Voort van Zyp, M. S. Hoogeman, S. van de Water, *et al.*, "Clinical introduction of monte carlo treatment planning: A different prescription dose for non-small cell lung cancer according to tumor location and size," *Radiotherapy and Oncology*, vol. 96, no. 1, pp. 55–60, 2010, ISSN: 0167-8140. DOI: https://doi.org/10.1016/j.radonc.2010.04.009.

[13] M. B. Liu, N. C. Eclov, N. Trakul, *et al.*, "Clinical impact of dose overestimation by effective path length calculation in stereotactic ablative radiation therapy of lung

tumors," *Practical Radiation Oncology*, vol. 3, no. 4, pp. 294–300, 2013, ISSN: 1879-8500. DOI: https://doi.org/10.1016/j.prro.2012.09.003.

[14] V. W. Wu, K.-w. Tam, and S.-m. Tong, "Evaluation of the influence of tumor location and size on the difference of dose calculation between ray tracing algorithm and fast monte carlo algorithm in stereotactic body radiotherapy of non-small cell lung cancer using cyberknife," *Journal of Applied Clinical Medical Physics*, vol. 14, no. 5, pp. 68–78, 2013. DOI: 10.1120/jacmp.v14i5.4280.

[15] S. E. Braunstein, S. A. Dionisio, M. W. Lometti, *et al.*, "Evaluation of ray tracing and monte carlo algorithms in dose calculation and clinical outcomes for robotic stereotactic body radiotherapy of lung cancers," *J Radiosurg SBRT*, vol. 3, no. 1, pp. 67–79, 2014, ISSN: 2156-4639.

[16] I. Kawrakow and D. W.O. Rogers, "The egsnrc code system: Monte carlo simulation of electron and photon transport," Jan. 2000.

[17] F. Araki, "Monte carlo study of a cyberknife stereotactic radiosurgery system," *Medical Physics*, vol. 33, no. 8, pp. 2955–2963, 2006. DOI: 10.1118/1.2219774.

[18] *Dosimetry of Small Static Fields Used in External Beam Radiotherapy*, ser. Technical Reports Series 483. Vienna: INTERNATIONAL ATOMIC ENERGY AGENCY, 2017, ISBN: 978-92-0-105916-1.

[19] H. H. Liu, P. Keall, and W. R. Hendee, "Rather than should be used in monte carlo treatment planning," *Medical Physics*, vol. 29, no. 5, pp. 922–924, 2002. DOI: 10.1118/1.1473137.

[20] P. Andreo, "Dose to 'water-like' media or dose to tissue in MV photons radiotherapy treatment planning: Still a matter of debate," *Physics in Medicine and Biology*, vol. 60, no. 1, pp. 309–337, Dec. 2014. DOI: 10.1088/0031-9155/60/1/309.

[21] C.-M. Ma and J. Li, "Dose specification for radiation therapy: Dose to water or dose to medium?" *Physics in Medicine and Biology*, vol. 56, no. 10, pp. 3073–3089, Apr. 2011. DOI: 10.1088/0031-9155/56/10/012.

[22] N. Reynaert, F. Crop, E. Sterpin, I. Kawrakow, and H. Palmans, "On the conversion of dose to bone to dose to water in radiotherapy treatment planning systems," *Physics and Imaging in Radiation Oncology*, vol. 5, pp. 26–30, 2018, ISSN: 2405-6316. DOI: https://doi.org/10.1016/j.phro.2018.01.004.

[23] M. Barton, "Tables of equivalent dose in 2 gy fractions: A simple application of the linear quadratic formula," *International Journal of Radiation Oncology*Biology*Physics*, vol. 31, no. 2, pp. 371–378, 1995, The Faculty of Radiation Oncology of The Royal Australasian College of Radiologists, ISSN: 0360-3016. DOI: https://doi.org/10.1016/0360-3016(94)E0126-5.

[24] J. M. Fernández-Varea, P. Carrasco, V. Panettieri, and L. Brualla, "Monte carlo based water/medium stopping-power ratios for various ICRP and ICRU tissues," *Physics in Medicine and Biology*, vol. 52, no. 21, pp. 6475–6483, Oct. 2007. DOI: 10.1088/0031-9155/52/21/009.

[25] T. Lacornerie, A. Lisbona, X. Mirabel, E. Lartigau, and N. Reynaert, "Gtv-based prescription in sbrt for lung lesions using advanced dose calculation algorithms," *Radiation Oncology*, vol. 9, no. 1, p. 223, Oct. 2014, ISSN: 1748-717X. DOI: 10.1186/s13014-014-0223-5.

[26] Y. Xiao, L. Papiez, R. Paulus, *et al.*, "Dosimetric evaluation of heterogeneity corrections for rtog 0236: Stereotactic body radiotherapy of inoperable stage i-ii non-small-cell lung cancer," *Int J Radiat Oncol Biol Phys*, vol. 73, no. 4, pp. 1235–1242, Mar. 2009, S0360-3016(08)03800-5[PII], ISSN: 1879-355X. DOI: 10.1016/j.ijrobp.2008.11.019.

CHAPTER 4
Correlation between dose distal to the target and distant metastasis incidence rate for CyberKnife lung patients

4.1 Preface

In addition to establishing the relation between target doses and loco-regional outcomes, the large set of recalculated lung dose distributions allowed us to investigate another recent clinical question. In a previous study by Diamant et al.[1], it was found that the dose delivered to regions proximally outside the PTV was inversely correlated with the incidence rate of Distant Metastasis (DM) in lung SBRT patients. The study was based on a patient cohort of 217 stage I NSCLC patients treated with conventional linacs (either Volumetric Arc Therapy (VMAT) or 3D Conformal Radiation Therapy (CRT)). In particular, they had found that patients receiving an EQD2 larger than 21 Gy in the region extending from the PTV to 30 mm beyond had a significantly lower incidence of DM. Patients receiving less than 21 Gy in that region had a worse DM-free survival rate with a hazard ratio of 24.2 (95%CI: 10.7, 54.4).

In this chapter, we aimed to determine the presence or absence of this correlation in CyberKnife lung patients. CyberKnife dose distributions differ from conventional linac mainly due to their non-coplanarity. In CyberKnife treatments, radiation beams can be delivered from almost any angles whereas VMAT or CRT plans are restricted to angles of an arc. The following study thus investigates whether or not the above correlation still holds for non-coplanar dose delivery.

The work described in this chapter is part of a study featured in a manuscript submitted for publication: A. Diamant[1] , V.J. Heng[1] , A. Chatterjee, S. Faria, H. Bahig, E. Filion, R. Doucet, I. El Naqa, J. Seuntjens, Does non-coplanar radiotherapy reduce distant recurrence in NSCLC patients compared to conventional SBRT? Manuscript submitted for publication (2019) [2].

4.2 Methods

The same patient cohort as described in Chapter 3 was used for this analysis with a few additional requirements. Only patients with a single lesion, and that had not received other CyberKnife lung treatments in the past 5 years were included in this study. Furthermore, only patients that were either followed-up for more than 12 months or had developed distant metastasis were considered. The final cohort for this part of the study was thus 205 stage I NSCLC patients. Dose prescription, planning and treatment specifications are the same as described in Chapter 3.

Only the recalculated MC dose distribution obtained in Chapter 3 was used in this analysis. For every patients, the dose in all voxels were converted to EQD2 with an α/β ratio of 10 Gy. The dose fall-off beyond the PTV was characterised by calculating the average dose in shells extending beyond the PTV. These shells will henceforth be called $\mathrm{ROI}_{\mathrm{cont}}(x)$, representing the continuous region of interest extending x mm away from the PTV. To create the $\mathrm{ROI}_{\mathrm{cont}}(x)$, a 3D convex hull of the PTV was generated from its contour points. The coordinate of the centroid of the hull was calculated as the mean coordinate of all hull points in each dimension. Each point of the hull was then extended x mm in the direction of the vector joining the centroid to the hull point. This results in a second larger convex hull. All lung voxels that lie between the two hulls constitute the $\mathrm{ROI}_{\mathrm{cont}}(x)$, see Fig.4–1. Voxels outside the lung contour were excluded so as to not consider the dose outside the patient

[1] co-first author

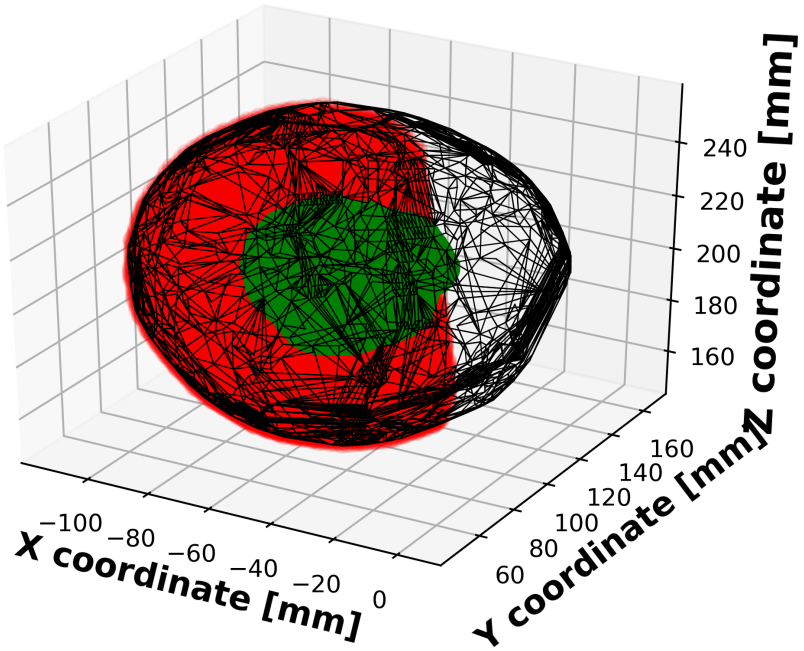

Figure 4–1: Example of the generation of a $\mathrm{ROI}_{\mathrm{cont}}(x)$. The green region corresponds to voxels inside the PTV. Black lines refer to the convex hull grown isotropically about the PTV. The red region corresponds to the $\mathrm{ROI}_{\mathrm{cont}}(x)$: all voxels that are both inside the lung and between the PTV and the grown hull.

body. The mean dose to voxels in the $\mathrm{ROI}_{\mathrm{cont}}(x)$ was then calculated. This process was repeated for every patient and for $x = 1$ to 100 mm.

The dose fall-off curve can be plotted as the mean dose to the $\mathrm{ROI}_{\mathrm{cont}}(x)$ as a function of the distance x from the PTV. This curve was averaged among patients who had developed DM and among patients who did not. A Wilcoxon rank sum test was performed for each $\mathrm{ROI}_{\mathrm{cont}}(x)$ to test for a statistically significant difference, defined at a p-value of 0.05, between the dose fall-off curve of the two subsets.

In the previous study, a significantly different DM-free survival curve was found for patients receiving doses either larger or lower than 21 Gy to the $\mathrm{ROI}_{\mathrm{cont}}(30)$. It was therefore interesting to compare the distribution of patient doses with respect to the previous threshold dose. The dose fall-off curve for the entire CyberKnife cohort was compared to the fall-off

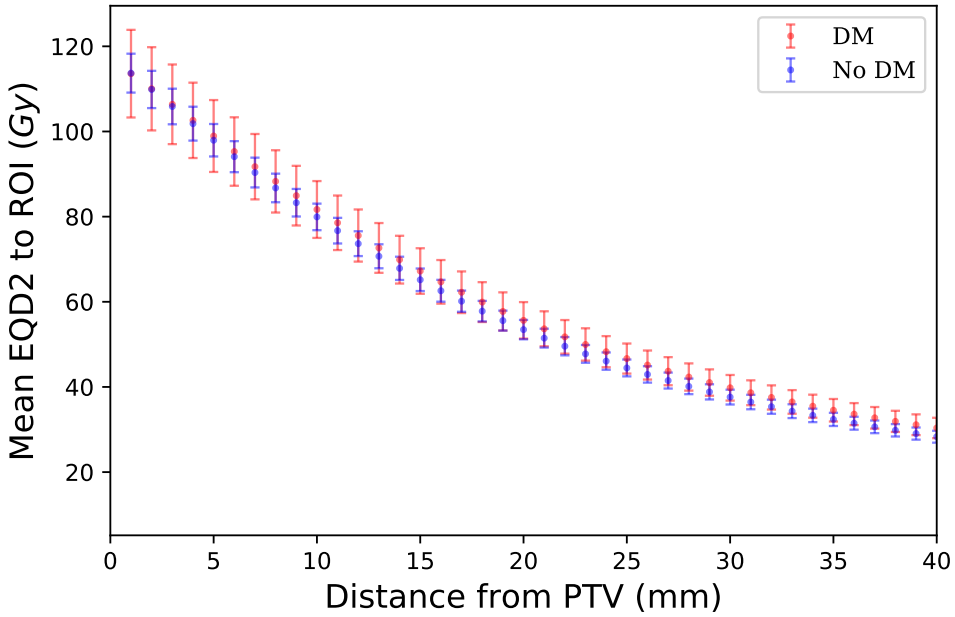

Figure 4–2: The mean dose to $\mathrm{ROI}_{\mathrm{cont}}(x)$ as a function of distance x beyond the PTV from 1 to 40 mm. The red points represent the mean dose averaged over patients who developed DM while blue points are averaged over patients who did not have DM. The error bars are calculated as the standard error on the subset-averaged mean with $k = 2$. Thus both curves overlap each other at the 95% confidence level.

curve of the patient cohort of the previous study (VMAT/CRT). The 95% confidence bands for both fall-off curves was calculated from the standard error on the cohort-mean of the mean dose to each $\mathrm{ROI}_{\mathrm{cont}}(x)$. A histogram representing the distribution of the mean dose to $\mathrm{ROI}_{\mathrm{cont}}(30)$ was plotted for the CyberKnife patient cohort with respect to the threshold dose of 21 Gy. The former was also compared to the VMAT/CRT distribution of the previous study.

4.3 Results

The mean dose to each ROI is plotted in Fig.4–2 for patients who developed DM and for patient who did not. The two dose fall-off curves are not distinguishable at the 95% confidence level. The Wilcoxon rank sum test did not find the dose to any $\mathrm{ROI}_{\mathrm{cont}}(x)$ to be statistically significantly different between patients with or without distant recurrences for

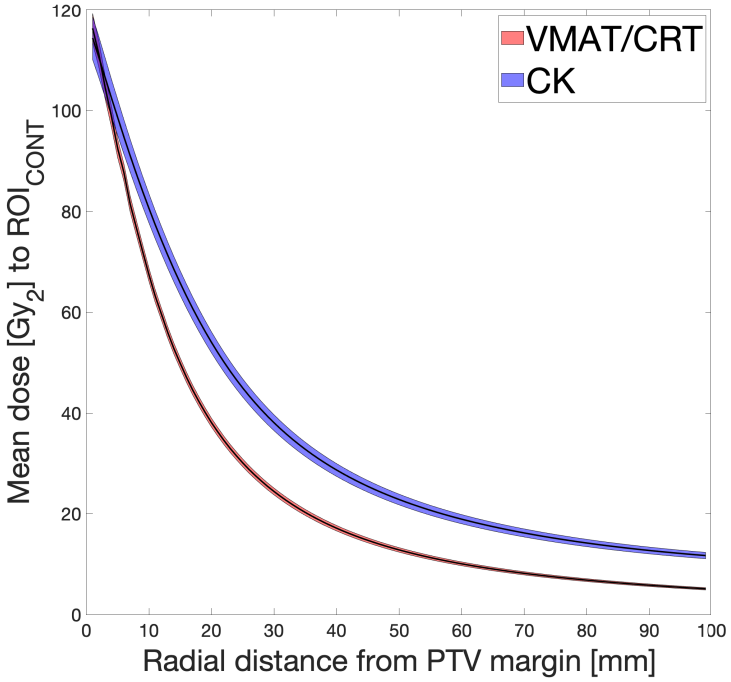

Figure 4–3: The mean EQD2 to ROI as a function of distance x from the PTV. The dose to regions outside the PTV in CyberKnife plans (blue) is significantly larger than VMAT/CRT plans (red) for $x > 10$ mm, despite having similar dose in the PTV at the 95% confidence level. This figure is extracted from [2], where Gy_2 is a Gy in EQD2.

any x between 1 and 100 mm ($p > 0.06$).

The dose fall-off curve beyond the PTV for the entire CyberKnife cohort and for the VMAT/CRT cohort is plotted in Fig.4–3. The dose fall-off in CyberKnife plans was found to be significantly slower than in VMAT/CRT plans at 95% confidence level. The average dose to all $\text{ROI}_{\text{cont}}(x)$ for $x > 10$ mm is significantly larger in CyberKnife plans.

When looking at the distribution of dose to $\text{ROI}_{\text{cont}}(x)$ for $x = 30$ mm beyond the PTV (Fig.4–4), 95% of all CyberKnife plans in this study were found to have a larger mean EQD2 to the $\text{ROI}_{\text{cont}}(30)$ than the threshold dose of 21 Gy determined in our previous work[1]. This is in stark contrast with the VMAT/CRT cohort, where only 75% of plans had a larger-than-threshold dose. The distribution of CyberKnife doses in Fig.4–4 is also observed to be more spread out, with maximum doses extending up to 71 Gy. The two distribution are found to have a significantly different median by the Wilcoxon rank sum test, with $p < 10^{-8}$.

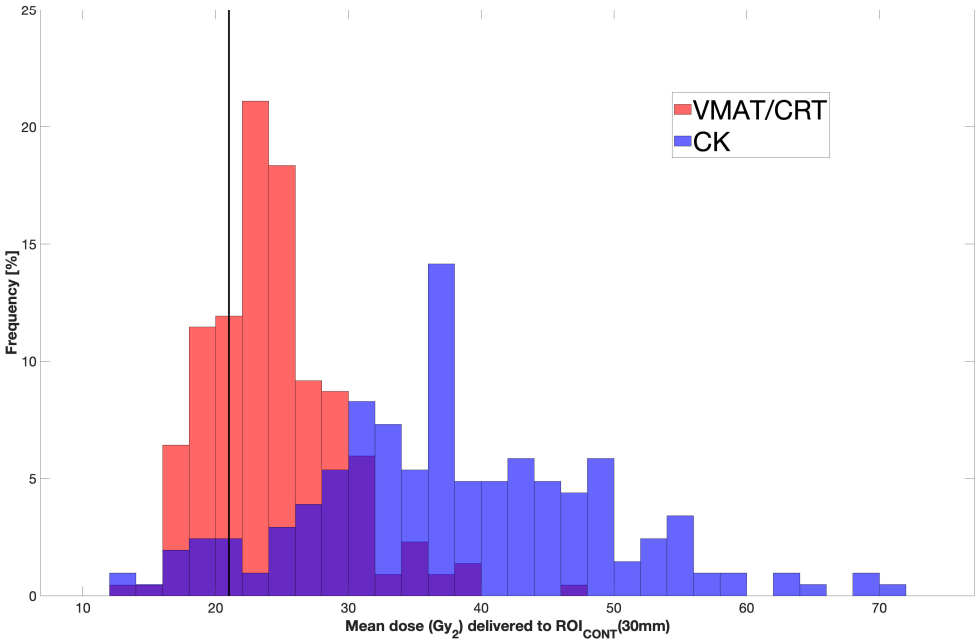

Figure 4–4: Histogram of the mean EQD2 to $\mathrm{ROI}_{\mathrm{cont}}(30)$ for CyberKnife (blue) and VMAT/CRT (red) plans. The threshold dose hypothesized in the previous study is represented by a black line. This figure is extracted from [2].

4.4 Discussion

In the previous study by Diamant et al. (2018)[1], VMAT/CRT patients who had developed DM were found to have received a significantly lower dose outside the PTV than patients who did not have a distant recurrence. However, in the present study, when the same analysis was performed in Fig.4–2 for CyberKnife patients, no significant difference with respect to dose could be observed between the DM and no DM groups.

Although this result may seem to refute the hypothesis proposed by the previous study, they can be reconciled by looking at the scale of the dose fall-off for CyberKnife plans. Indeed, as shown in Fig.4–3, CyberKnife plans have a significantly slower dose fall-off outside the PTV than in VMAT/CRT plans, despite having similar doses near the PTV. Our hypothesis is that this is due to the non-coplanarity of the delivery. In conventional linac delivery, the dose distribution is concentrated on a few axial slices as the linac is rotated along an arc.

Beyond those slices, the dose falls off rapidly. As such, the only lung voxels in which the dose is non-negligible are those near the axial slices of the PTV (see Fig.4–5). By definition, the $\mathrm{ROI}_{\mathrm{cont}}(x)$ are isotropic expansions of the PTV (minus the PTV itself). For $x > 10$ mm beyond the PTV, the ROI will include an increasingly larger fraction voxels that are axially far enough from the PTV such that they have almost zero doses. In contrast, in CyberKnife treatments, the dose delivery can come from almost any angle (except from below the couch). As such, a larger fraction of the lung is susceptible to be in the path of the beam as shown in Fig.4–5. This thus leads to fewer lung voxels with negligible dose, thereby explaining the slower dose fall-off observed in Fig.4–3.

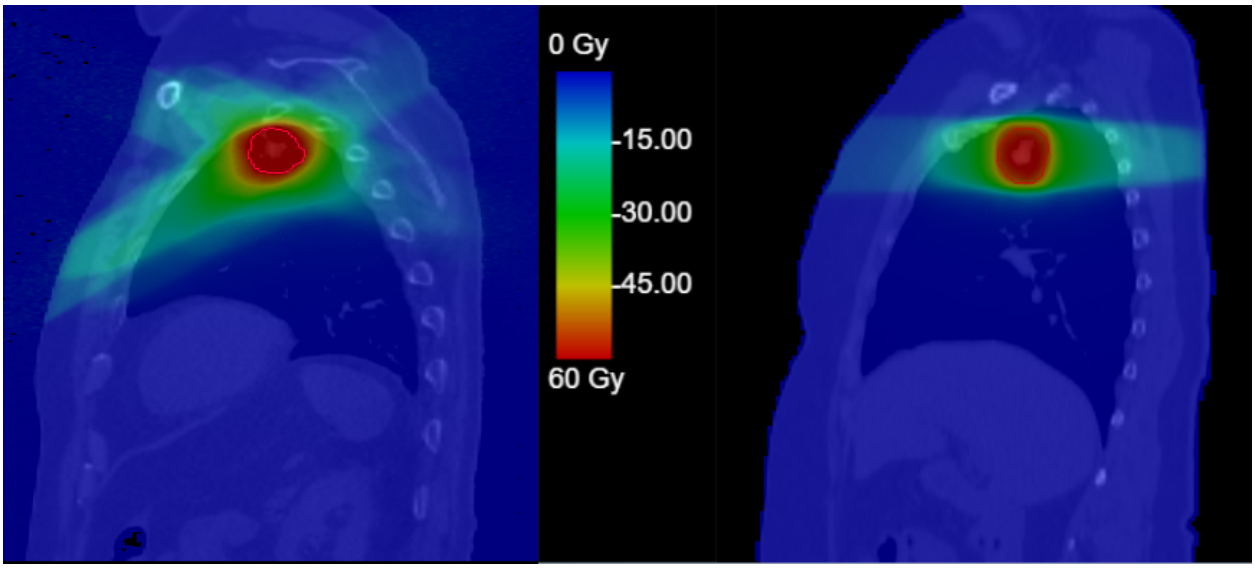

Figure 4–5: Sagittal slice of the dose distribution in a typical CyberKnife (left) vs. a CRT plan (right). The red contour represents the PTV. The dose in the CRT plan is limited to slices near the PTV. This figure was produced by viewing the patients' dose distribution on Radify.

Due to a slower dose-fall off, only 5% of CyberKnife plans were found to have an average dose to $\mathrm{ROI}_{\mathrm{cont}}(30)$ lower than the 21 Gy threshold dose. We hypothesize that no dosimetric distinction between DM and no DM patients were found because almost all the patients already belong to the higher-than-threshold branch. Assuming that DM control can be associated to a sigmoidal behavior of the TCP of microscopic disease extension, CyberKnife

lung plans would lie on the high dose plateau [2]. Variations in doses within the plateau would thus have negligible effects on DM control rates (see Fig.2–10). It thus logically follows that the CyberKnife patient cohort should be expected to have superior outcomes with respect to distant recurrences. This was found to be the case when the CyberKnife patients were compared to the low-dose branch of the VMAT/CRT patients from the previous study [2].

REFERENCES

[1] A. Diamant, A. Chatterjee, S. Faria, *et al.*, "Can dose outside the ptv influence the risk of distant metastases in stage i lung cancer patients treated with stereotactic body radiotherapy (sbrt)?" *Radiotherapy and Oncology*, vol. 128, no. 3, pp. 513–519, 2018, ISSN: 0167-8140. DOI: https://doi.org/10.1016/j.radonc.2018.05.012.

[2] A. Diamant, V. J. Heng, A. Chatterjee, *et al.*, "Does non-coplanar radiotherapy reduce distant recurrence in NSCLC patients compared to conventional SBRT," *Manuscript submitted for publication*, 2019.

CHAPTER 5
Conclusion

In this retrospective work, a full MC recalculation of a large set of 219 CyberKnife NSCLC plans was carried out. For this purpose, a beam model of the CyberKnife was built on BEAMnrc. The purpose of the recalculation was two-fold. First, it allowed an extensive assessment of the accuracy of the different TPS dose calculation methods in lung. While the TPS fast MC algorithm showed good agreement with our full MC, a large discrepancy was observed for the RAT algorithm. When tissue heterogeneities were accounted for with densities obtained from a proper CT-density curve, RAT was found to consistently overestimate the dose in the PTV. This overestimation is in agreement with past literature. However, if no tissue heterogeneity corrections were used, such that all voxel above a threshold CT number were considered to have unit density, the discrepancy in target dose calculated by RAT and by MC becomes highly variable and less predictable. With a decade of research having shown the failure of RAT in lung calculations, it is now common practice to calculate CyberKnife lung plans using the MC method. Nevertheless, most of the clinical experience has been based on RAT-calculated doses. As early lung SBRT clinical trials [1], [2] required patients to be planned without heterogeneity corrections, our results suggest that their findings on the appropriate prescription dose may not be simply translated to MC calculations. Plausible workarounds have been suggested to match MC-based prescription doses to the prior RAT-based prescriptions. Indeed, van der Voort van Zyp et al. had proposed to scale down prescription doses for smaller tumors [3]. Lacornerie et al. suggested to renormalize the MC-calculated dose distribution such that the median GTV dose equals the prescription dose [4]. These suggestions however do not take into account the inaccurate attenuation due to the lack of heterogeneity corrections.

In addition, the recalculation was used to investigate the correlation between MC-calculated doses and loco-regional and distant outcomes. The coverage of the target by the original prescription dose was found to be a poor predictor of loco-regional control. Instead, it was the coverage by an absolute dose that was positively correlated with loco-regional control rates. On the other hand, the dose outside the PTV was not found to be predictive of DM incidence rates, in stark contrast to the strong correlation observed by Diamant et al. [5] in linac-delivered SBRT patients. This is hypothesized to be due to the significantly larger dose outside the PTV in CyberKnife patients compared to VMAT/CRT patients. Within this framework, no significant distinction in DM incidence rates would be expected among patients receiving doses higher than a threshold.

Although this explanation may reconcile the lack of correlation with the previous study, the present study in itself does not corroborate the hypothesis of a predictive dose region beyond the PTV with respect to distant recurrences. As such, the above hypothesis remains to be confirmed in an independent set of linac-delivered lung SBRT patients. However, if such a correlation can be independently demonstrated to be present, the results of this study would indicate that non-coplanar dose distribution, due to their slower isotropic dose fall-off, are inherently better suited at controlling distant recurrences. As distant metastasis is associated with a significantly worse prognosis in NSCLC patients [6], it would therefore be of interest to revisit prescription methods in linac-delivered SBRT treatments such as to deliver higher doses isotropically around the PTV.

An exciting direction for future work on dose-to-outcome modelling resides in machine learning approaches. Rather than using statistical tests and fits to infer correlation between parameters, one can train a neural network to associate dose patterns to their patient outcomes. As we have found that higher MC-calculated PTV doses were correlated with better loco-regional control rates, a neural network could be used to predict the likelihood of recurrences based on the dose distribution that will be delivered.

In conclusion, this work has demonstrated the necessity of using advanced type-b methods for accurate dose calculation in the lung. This is all the more true as delivering a sufficient dose to the target is observed to lead to fewer local recurrences. As correlations between dose and outcomes were investigated, this work also highlights the importance of using accurate doses as the basis for a dose-to-outcome model.

REFERENCES

[1] R. Timmerman, R. Paulus, J. Galvin, *et al.*, "Stereotactic Body Radiation Therapy for Inoperable Early Stage Lung Cancer," *JAMA*, vol. 303, no. 11, pp. 1070–1076, Mar. 2010, ISSN: 0098-7484. DOI: 10.1001/jama.2010.261.

[2] R. D. Timmerman, R. Paulus, H. I. Pass, *et al.*, "Stereotactic Body Radiation Therapy for Operable Early-Stage Lung Cancer: Findings From the NRG Oncology RTOG 0618 Trial Stereotactic Body Radiation Therapy for Operable Early-Stage Lung Cancer Stereotactic Body Radiation Therapy for Operable Early-Stage Lung Cancer," *JAMA Oncology*, vol. 4, no. 9, pp. 1263–1266, Sep. 2018, ISSN: 2374-2437. DOI: 10.1001/jamaoncol.2018.1251.

[3] N. C. van der Voort van Zyp, M. S. Hoogeman, S. van de Water, *et al.*, "Clinical introduction of monte carlo treatment planning: A different prescription dose for non-small cell lung cancer according to tumor location and size," *Radiotherapy and Oncology*, vol. 96, no. 1, pp. 55–60, 2010, ISSN: 0167-8140. DOI: https://doi.org/10.1016/j.radonc.2010.04.009.

[4] T. Lacornerie, A. Lisbona, X. Mirabel, E. Lartigau, and N. Reynaert, "Gtv-based prescription in sbrt for lung lesions using advanced dose calculation algorithms," *Radiation Oncology*, vol. 9, no. 1, p. 223, Oct. 2014, ISSN: 1748-717X. DOI: 10.1186/s13014-014-0223-5.

[5] A. Diamant, A. Chatterjee, S. Faria, *et al.*, "Can dose outside the ptv influence the risk of distant metastases in stage i lung cancer patients treated with stereotactic body radiotherapy (sbrt)?" *Radiotherapy and Oncology*, vol. 128, no. 3, pp. 513–519, 2018, ISSN: 0167-8140. DOI: https://doi.org/10.1016/j.radonc.2018.05.012.

[6] SEER. (2018). Cancer of the lung and bronchus - cancer stat facts, [Online]. Available: https://seer.cancer.gov/statfacts/html/lungb.html (visited on 07/29/2019).